

REPORT DOCUMENTATION PAGE

Form Approved
OMB No. 0704-0188

Public reporting burden for this collection of information is estimated to average 1 hour per response, including the time for reviewing instructions, searching existing data sources, gathering and maintaining the data needed, and completing and reviewing this collection of information. Send comments regarding this burden estimate or any other aspect of this collection of information, including suggestions for reducing this burden to Department of Defense, Washington Headquarters Services, Directorate for Information Operations and Reports (0704-0188), 1215 Jefferson Davis Highway, Suite 1204, Arlington, VA 22202-4302. Respondents should be aware that notwithstanding any other provision of law, no person shall be subject to any penalty for failing to comply with a collection of information if it does not display a currently valid OMB control number. **PLEASE DO NOT RETURN YOUR FORM TO THE ABOVE ADDRESS.**

1. REPORT DATE (DD-MM-YYYY) 05-09-2014		2. REPORT TYPE		3. DATES COVERED (From - To)	
4. TITLE AND SUBTITLE		An Analysis of the Loads on and Dynamic Response of a Floating Flexible Tube in Waves and Currents		5a. CONTRACT NUMBER	
				5b. GRANT NUMBER	
				5c. PROGRAM ELEMENT NUMBER	
6. AUTHOR(S) Genzman, Grant Norman				5d. PROJECT NUMBER	
				5e. TASK NUMBER	
				5f. WORK UNIT NUMBER	
7. PERFORMING ORGANIZATION NAME(S) AND ADDRESS(ES)				8. PERFORMING ORGANIZATION REPORT NUMBER	
9. SPONSORING / MONITORING AGENCY NAME(S) AND ADDRESS(ES) U.S. Naval Academy Annapolis, MD 21402				10. SPONSOR/MONITOR'S ACRONYM(S)	
				11. SPONSOR/MONITOR'S REPORT NUMBER(S) Trident Scholar Report no. 427 (2014)	
12. DISTRIBUTION / AVAILABILITY STATEMENT This document has been approved for public release; its distribution is UNLIMITED.					
13. SUPPLEMENTARY NOTES					
14. ABSTRACT Proposed offshore structure designs for algal production using wastewater may incorporate floating flexible tubes. This study includes an extensive set of physical modeling experiments to investigate the loads on and dynamic response of these tubes in waves and currents. The physical modeling approach involved designing and building an approximately 1:4 scaled representation of a potential design. Experiments were conducted with the model in the 37-meter tow/wave tank in Hydromechanics Laboratory at the United States Naval Academy. Several combinations of model tests were performed in scaled waves and currents at tube fill levels of 50% and 95%. Several of the tow tests done in the tank, representing oceanic currents, were validated with computational fluid dynamics. Along with the time series drag results, the physical modeling experiments that included both regular and random waves were analyzed to produce linear transfer functions for both heave and force. An assessment of these data sets indicated that the flexible floating tube response generally followed the wave forcing at the middle wave frequencies. For both fill levels, the response of the forward end of model increased with wave frequency while the response of the rear end of the model remained rather consistent across the frequencies tested. The results did not indicate a significant difference in dynamic response when the model was tested in both waves and current. The average attachment loads, however, were higher when the model was tested in waves and a current than in waves only.					
15. SUBJECT TERMS Flexible tube; Response amplitude operator; Hydromechanics; Computational fluid dynamics					
16. SECURITY CLASSIFICATION OF:		17. LIMITATION OF ABSTRACT	18. NUMBER OF PAGES 79	19a. NAME OF RESPONSIBLE PERSON	
a. REPORT	b. ABSTRACT			c. THIS PAGE	19b. TELEPHONE NUMBER (include area code)

**AN ANALYSIS OF THE LOADS ON AND DYNAMIC RESPONSE OF A FLOATING
FLEXIBLE TUBE IN WAVES AND CURRENTS**

by

Midshipman 1/c Grant N. Genzman
United States Naval Academy
Annapolis, Maryland

(signature)

Certification of Adviser(s) Approval

Associate Professor David W. Fredriksson
Naval Architecture and Ocean Engineering Department

(signature)

(date)

Professor Michael P. Schultz
Naval Architecture and Ocean Engineering Department

(signature)

(date)

Acceptance for the Trident Scholar Committee

Professor Maria J. Schroeder
Associate Director of Midshipman Research

(signature)

(date)

Abstract

Proposed offshore structure designs for algal production using wastewater may incorporate floating flexible tubes. This study includes an extensive set of physical modeling experiments to investigate the loads on and dynamic response of these tubes in waves and currents. The physical modeling approach involved designing and building an approximately 1:4 scaled representation of a potential design. Experiments were conducted with the model in the 37-meter tow/wave tank in Hydromechanics Laboratory at the United States Naval Academy. Several combinations of model tests were performed in scaled waves and currents at tube fill levels of 50% and 95%. Several of the tow tests done in the tank, representing oceanic currents, were validated with computational fluid dynamics.

Along with the time series drag results, the physical modeling experiments that included both regular and random waves were analyzed to produce linear transfer functions for both heave and force. An assessment of these data sets indicated that the flexible floating tube response generally followed the wave forcing at the middle wave frequencies. For both fill levels, the response of the forward end of model increased with wave frequency while the response of the rear end of the model remained rather consistent across the frequencies tested.

The results did not indicate a significant difference in dynamic response when the model was tested in both waves and current. The average attachment loads, however, were higher when the model was tested in waves and a current than in waves only. The attachment loads were also higher in wave and current conditions that included a faster current or lower-frequency (larger) waves.

Keywords: Flexible tube; Response amplitude operator; Hydromechanics; Computational fluid dynamics

Acknowledgements

I would like to express my sincere gratitude to all of the professionals in the Hydromechanics Laboratory – without their expertise and assistance, none of this project could have been accomplished. I am also grateful for and would like to thank my co-advisors, Associate Professor David Fredriksson and Professor Michael Schultz, for their exceptional support, guidance, and instruction. A special thank you also goes to Dr. Jonathan Trent of NASA Ames Research Center for his many interesting discussions and guidance early on and continuing throughout this project.

Table of Contents

Abstract	1
Acknowledgements	2
Table of Contents	3
Table of Figures	6
Table of Tables	11
1 Introduction	12
2 Theoretical Review and Data Processing	15
2.1 Fluid Dynamic Drag	15
2.2 Response Amplitude Operators (RAOs)	16
2.2.1 Regular Wave RAOs	17
2.2.2 Irregular Wave RAOs	18
2.2.3 RAO Data Processing	19
2.3 Uncertainty Analysis	20
3 Physical Modeling Experiments	22
3.1 Overview	22
3.2 Scaling Approach	23
3.2.1 Theory	23
3.2.2 Procedure	25
3.2.3 Physical Model Scaling Results	26

3.3	Experiment Setup	27
3.4	Testing Procedure.....	31
4	Computational Fluid Dynamics	33
5	Results and Discussion	37
5.1	Model and Simulation Results in Currents	37
5.2	Free-End Attachment	38
5.2.1	Drag Tests	38
5.2.2	Wave Tests, 3MIL Model	39
5.2.3	Wave Tests, 6MIL Model	46
5.2.4	Waves and Current Tests	51
5.3	Fixed-End Attachment	55
5.3.1	Drag Tests	55
5.3.2	Wave Tests.....	56
5.3.3	Waves and Current Tests	61
5.4	Overall Results	65
5.4.1	Drag Coefficients	65
5.4.2	Wave Tests.....	65
5.4.3	Wave and Current Tests.....	70
6	Conclusions.....	75
6.1	Overview	75

6.2	Generalized Results.....	75
6.3	Design Suggestions and Future Work.....	75
7	References.....	77
8	Appendix A – Nomenclature	79

Table of Figures

Figure 1: Conceptual design of a coastal outfall attachment using floating flexible tubes.	12
Figure 2: 37-meter tank experiment setup	27
Figure 3: The experiment setup showing the model in the water attached to the force block at the front of the carriage and the strain gages attached to each end cap with a spring and fishing line.	28
Figure 4: Tube end caps	29
Figure 5: Free-end attachment with the inextensible tow-line.....	30
Figure 6: Fixed-end attachment with the tube directly attached to a pipe structure.....	30
Figure 7: Energy spectral density of JONSWAP irregular wave input spectrum.	32
Figure 8: CFD Model of 100% Full Tube	33
Figure 9: CFD Model of 50% Full Tube	34
Figure 10: Computational Mesh and Flow Field for 100% Full CFD Model	35
Figure 11: Computational Mesh and Flow Field for 50% Full CFD Model	36
Figure 12: Drag coefficients from CFD simulations and Hoerner [11] accross a range of Reynolds numbers from $Re=10$ to $Re=10^7$	37
Figure 13: Free-end drag test results from both the physical model tests and CFD. The dotted and solid lines are the curve fit values of the individual tests (points) in the series.....	38
Figure 14: Free-end 3 MIL model response in waves (50% full). The solid line and the circle points represent the response of the forward end cap in irregular and regular waves, respectively. The dashed line and asterisks represent the response of the rear end cap in irregular and regular waves, respectively.	40

Figure 15: Free-end 3 MIL model response in waves (95% full). The solid line and the circle points represent the response of the forward end cap in irregular and regular waves, respectively. The dashed line and asterisks represent the response of the rear end cap in irregular and regular waves, respectively.	41
Figure 16: Free-end attachment loads on 95% full model in irregular waves.	43
Figure 17: Free-end 3 MIL model response in waves (50% full). The solid line represents the spectral tension RAO. The circle points represent the average tension RAO, the asterisks represent the standard deviation RAO, and the square points represent the sum of the previous two values.	44
Figure 18: Free-end 3 MIL model response in waves (95% full). The solid line represents the spectral tension RAO. The circle points represent the average tension RAO, the asterisks represent the standard deviation RAO, and the square points represent the sum of the previous two values.	45
Figure 19: Free-end 6 MIL model response in waves (50% full). The solid line and the circle points represent the response of the forward end cap in irregular and regular waves, respectively. The dashed line and asterisks represent the response of the rear end cap in irregular and regular waves, respectively.	47
Figure 20: Free-end 6 MIL model response in waves (95% full). The solid line and the circle points represent the response of the forward end cap in irregular and regular waves, respectively. The dashed line and asterisks represent the response of the rear end cap in irregular and regular waves, respectively.	48
Figure 21: Free-end 6 MIL model response in waves (50% full). The solid line represents the spectral tension RAO. The circle points represent the average tension RAO, the asterisks	

represent the standard deviation RAO, and the square points represent the sum of the previous two values.....	49
Figure 22: Free-end 6 MIL model response in waves (95% full). The solid line represents the spectral tension RAO. The circle points represent the average tension RAO, the asterisks represent the standard deviation RAO, and the square points represent the sum of the previous two values.....	50
Figure 23: Wave only RAOs v. wave and current RAOs. Each graph presents the same sets of wave/current conditions. The top graphs show 50% full (a, b) and the bottom show 95% full (c, d). The left graphs (a, c) show the front end cap response and the right graphs (b, d) show the rear end cap response. The three symbols stacked at the same frequency represent three different current speeds (0.12, 0.30, and 0.49 m/s) tested with waves of that particular frequency. The asterisks represent tests of waves only.....	52
Figure 24: Attachment loads on free-end model filled to 50% and 95% in waves only (thick lines) and waves and current (thin lines). The circle points represent the average load and the asterisk points represent the standard deviation of the load measurements for each current velocity.....	53
Figure 25: Fixed-end drag test results from both the physical model tests and CFD. The dotted and solid lines are the curve fit values of the individual tests (points) in the series.....	55
Figure 26: Fixed-end 3 MIL model response in waves (50% full). The dashed line and asterisks represent the response of the rear end cap in irregular and regular waves, respectively.....	57
Figure 27: Free-end 3 MIL model response in waves (95% full). The dashed line and asterisks represent the response of the rear end cap in irregular and regular waves, respectively.....	58

Figure 28: Fixed-end 3 MIL model response in waves (50% full). The solid line represents the spectral tension RAO. The circle points represent the average tension RAO, the asterisks represent the standard deviation RAO, and the square points represent the sum of the previous two values.....	59
Figure 29: Fixed-end 3 MIL model response in waves (95% full). The solid line represents the spectral tension RAO. The circle points represent the average tension RAO, the asterisks represent the standard deviation RAO, and the square points represent the sum of the previous two values.....	60
Figure 30: Wave only RAOs v. wave and current RAOs. Each graph presents the same sets of wave/current conditions. The top graph shows 50% full and the bottom shows 95% full. The three symbols stacked at the same frequency represent three different current speeds (0.12, 0.30, and 0.49 m/s) tested with waves of that particular frequency. The asterisks represent tests of waves only.....	62
Figure 31: Attachment loads on fixed-end model filled to 50% and 95% in waves only (thick lines) and waves and current (thin lines). The circle points represent the average load and the asterisk points represent the standard deviation of the load measurements for each current velocity.....	63
Figure 32: Wave-only RAOs for all situations. The solid lines and the circle points represent the response of the forward end cap in irregular and regular waves, respectively. The dashed lines and asterisks represent the response of the rear end cap in irregular and regular waves, respectively. Each individual graph displays results from a different fill level or attachment method.....	66

Figure 33: Forward end cap RAOs (left) and rear end cap RAOs (right). The blue lines represent 3 MIL models and the red lines represent 6 MIL models. The dashed lines represent models that are 50% full and the solid lines represent models that are 95% full.....	67
Figure 34: Rear RAOs with the addition of the RAOs from the fixed-end testing. The dashed and solid lines represent 50 and 95% fill levels, respectively. The blue and red lines represent 3 MIL and 6 MIL models, respectively. The green lines represent the results from the fixed-end model.....	68
Figure 35: Wave-only attachment load (tension) RAOs for all situations. The solid lines represent the spectral tension RAOs. The circle points represent the average tension RAO, the asterisks represent the standard deviation RAO, and the square points represent the sum of the previous two values. Each individual graph displays results from a different fill level or attachment method.....	69
Figure 36: Wave only RAOs v. wave and current RAOs. Each graph presents the same sets of wave/current conditions. The top graphs show 50% full (a, b, c) and the bottom show 95% full (d, e, f).....	71
Figure 37: Attachment loads on model in waves only (thick lines) and waves and current (thin lines). The circle points represent the average load and the asterisk points represent the standard deviation of the load measurements. Each graph shows tests with towing speeds of 0.12, 0.30, and 0.49 m/s.....	73

Table of Tables

Table 1: 37-meter Testing Tank Scaling Results Summary	27
Table 2: Measurement error for 3 MIL model with free-end attachment in waves.....	46
Table 3: Measurement error for 6 MIL model with free-end attachment in waves.....	51
Table 4: Measurement error for 3 MIL model with free-end attachment in waves and currents .	54
Table 5: Measurement error for 3 MIL model with fixed-end attachment in waves.....	61
Table 6: Measurement error for 3 MIL model with fixed-end attachment in waves and currents	64

1 Introduction

To meet future energy demands, the development of sustainable sources of energy is becoming more important. Especially useful are techniques that utilize often-abundant residuals to create energy. These residuals can include solid waste, agricultural runoff, and gases from garbage dumps, among others. One possible technique is to grow algae for biofuels in floating flexible tubes that are fed municipal wastewater from coastal wastewater outfalls. Aspects of this concept have been investigated, as discussed by Trent et al. [1], in a pilot project called OMEGA (Offshore Membrane Enclosure for Growing Algae). Figure 1 shows a potential design for the coastal production of algae biomass using municipal wastewater in floating flexible tubes.

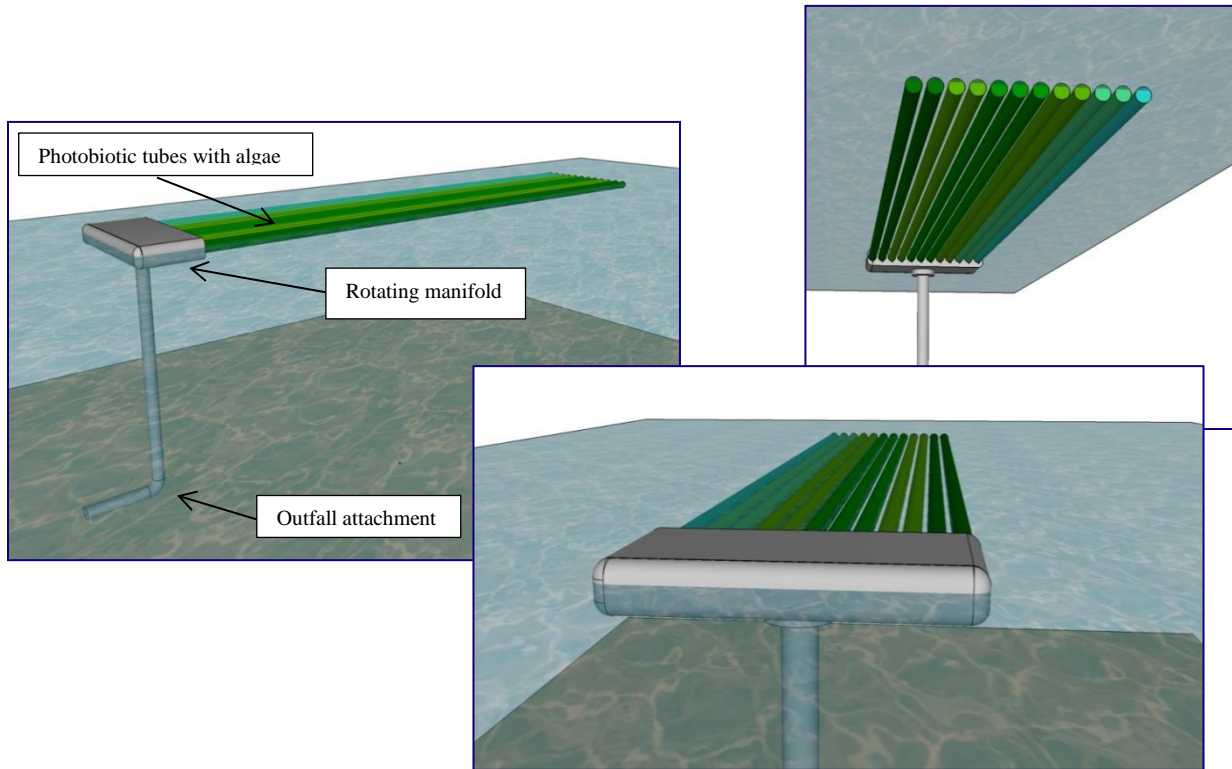


Figure 1: Conceptual design of a coastal outfall attachment using floating flexible tubes.

In the coastal or open ocean, the floating tubes will have to withstand environmental conditions including waves and currents, while maintaining structural integrity to contain water and algae. Understanding the loads on and the dynamic response of the system will be essential if this concept is to become useable. The development of both physical and computer modeling techniques is a necessary step in evaluating a design and preventing structural failure. The objective of this project was to investigate the dynamic nature of long flexible structures having different fill levels with both physical and numerical modeling techniques. Being able to predict the loads and responses will enhance the development of design procedures for use of these structures in the ocean environment.

Membranes used for transporting and storing fluids in the ocean have been considered since Hawthorne's concept of the Dracone Barge in 1961 [2]. The Dracone barge is a large flexible tube, sealed at both ends. The intent is to facilitate transportation of liquid cargo by submerging and towing the container behind a ship. Additionally, there has been work noting the particular challenges and considerations necessary when working with fabric as a construction material in the ocean environment. In particular, the benefit of physical modeling and testing for compliant structures such as membranes and nets has been expressed by Loland and Aarsnes [3]. Numerical and experimental analysis techniques have also been conducted with flexible fabric breakwater systems ([4], [5], [6]) and floating flexible tube structures ([2], [7], [8], [9], [10]). Most of these analyses focus on stresses in the material and the shape of the structure. The purpose of the work presented here was to investigate the attachment loads and response motions of a slender flexible tube at the surface through physical model testing and computational fluid dynamics (CFD).

A step-wise approach was taken to study the dynamics associated with long plastic tubes filled with water. Keeping the photobiotic premise in mind, a potential design concept with photobiotic tubes was developed (Figure 1). As shown on Figure 1, the design would include multiple tubes attached to a rotating manifold that connects to a portion of a wastewater outfall. In this case, the tube would be made of low linear density polyethylene (LLDPE) plastic with a length of 15.2 meters and a diameter of 20.3 centimeters. Physical models of the photobiotic tube were then designed by applying scale modeling techniques and constructed. The models were tested in the tank facilities in the Hydromechanics Laboratory at the United States Naval Academy at two internal fill levels and two attachment configurations. Physical model tests were conducted to represent oceanic currents, waves, and a combination of waves and currents. A complementary set of CFD simulations were done to assess drag characteristics under certain controlled conditions. Physical model tests were also performed to assess the dynamic response of the model due to waves and currents.

2 Theoretical Review and Data Processing

2.1 Fluid Dynamic Drag

Fluid dynamic drag can be categorized as the force (F_D) created through the interaction of a structure immersed in a fluid having a velocity (U), such that

$$F_D = \frac{1}{2} \rho A C_D U^2. \quad (1)$$

In Equation (1), ρ is the density of the fluid, A is the prescribed reference area, and C_D is the drag coefficient. Often, drag is separated into form drag and friction drag. Form drag is a function of the cross-sectional shape with the area (A) perpendicular to the flow. Friction drag comes from the friction of the parallel flow along a surface. In this case, the surface area of the object is used for A in Eq. (1).

When deploying an object in a specific environment, the density of the fluid and the reference area of the object will typically remain consistent. However, as the flow velocity increases or decreases, the drag force on the object changes with velocity squared. Similarly, the drag coefficient C_D is a function of Reynolds number,

$$Re = \frac{Ul}{\nu}, \quad (2)$$

where l is the characteristic dimension and ν is the kinematic viscosity. The value of C_D accounts for the shape of the object and the corresponding flow field characteristics. Drag coefficients for many common shapes are found in published material such as Hoerner [11]. In cases where drag coefficients are not available, they can be determined through physical model testing and numerical approaches.

In this study, drag coefficients were calculated from both the results of the physical and numerical modeling tests. The physical modeling data sets were obtained from towing the slender tube in the tow tank facility. The measurement data sets were obtained after the model

speed and response stabilized. The data time series were truncated to isolate 20-second periods where the model was moving at a desired steady speed. Using truncated data from six runs at each speed, averages of both towing speed and force were calculated. The output of the CFD software was more straightforward, providing both average flow speed and average total force.

For both modeling techniques, the resulting forces were plotted against the average towing speeds. Then a curve was fit to the data using a technique to minimize the error by finding an m-value that allowed the data to best fit the following equation form,

$$y = mx^2. \quad (3)$$

Curve fitting allows the experimental results to be compared to Eq. (1). In Eq. (3), the m-value then represents $\frac{1}{2}\rho A C_D$ of Eq. (1) and, by substituting values into Eq. (1), a value for the drag coefficient (C_D) was determined.

The CFD software was also used to investigate the influence of Reynolds number on the drag coefficient. Simulations were performed with the 100% full (solid) model with flow velocities that yielded Reynolds numbers from 10 to 10^7 . Drag coefficients were calculated for each simulation according to Eq. (1) and the results were plotted on a logarithmic plot against referenced drag coefficients for a similar model [11]. For comparison, physical model test results were also plotted on the log plot.

2.2 Response Amplitude Operators (RAOs)

Wind generated waves are another primary source of forcing on structures in the ocean that was addressed in this investigation. The energy from waves on an object can affect the heave (vertical), surge (horizontal), and pitch (rotational) motions of the object. The response of an object, especially a floating object, typically varies with the frequency and amplitude of the

wave forcing. In situations where the structure is being forced at the same frequency as the natural frequency, an increased dynamic response can often lead to increased loads at attachment points or mooring systems. One way to characterize the effect of waves on the response of the object is with the use of linear transfer functions. Such transfer functions are also called response amplitude operators (RAOs) and can be used to represent response as a function of wave forcing at various wave frequencies. This investigation uses a heave RAO (heave amplitude/wave elevation amplitude) and an attachment load RAO (attachment load/wave elevation amplitude) to characterize system response to waves of different frequencies, understanding that a transfer function for attachment tension may not be linear due to nonlinear drag forces.

2.2.1 Regular Wave RAOs

In this study, two types of heave RAO calculations were used to reflect the response of the tube in both regular and irregular waves. In single frequency regular waves, the heave RAO was calculated by normalizing the heave response amplitude with the incoming wave forcing amplitude,

$$H_{Regular} = \frac{\text{Heave Amplitude}}{\text{Wave Amplitude}}, \quad (4)$$

which can be done at a range of wave frequencies.

Additionally, three tension RAOs were calculated using average attachment load ($RAO_{AveForce}$), the amplitude of the attachment load ($RAO_{StDevForce}$), and the total attachment force ($RAO_{TotalForce}$) as follows:

$$RAO_{AveForce} = \frac{\text{Average Tension}}{\text{Wave Amplitude}}, \quad (5)$$

$$RAO_{StDevForce} = \frac{\text{Tension Amplitude}}{\text{Wave Amplitude}}, \quad (6)$$

and

$$\text{RAO}_{\text{TotalForce}} = \frac{\text{Total Tension}}{\text{Wave Amplitude}}, \quad (7)$$

which were also done at a range of wave frequencies. The total tension force used in Eq. (7) was calculated as the sum of the average tension and the standard deviation of the tension for each wave frequency.

2.2.2 Irregular Wave RAOs

Irregular wave profiles (η) are composed of a superposition of multiple frequency components (f), each with a distinct amplitude (a) and phase (φ) such that,

$$\eta(t) = \sum_{i=1}^N a_i \cos(2\pi f_i t - \varphi_i). \quad (8)$$

Irregular wave data sets can be represented as a distribution of square amplitudes per frequency bin such that the area under the spectral curve is equal to the variance. This distribution is often called an energy density spectrum. Recorded time series data sets are represented in the frequency domain with a one-sided energy density spectrum, $G(f)$, which is discretized according to

$$G_\eta(f) = \frac{2\{(xf)[\text{conj}(xf)]\}}{[(\text{rate})(n)]}. \quad (9)$$

In Equation (9), xf is the Fast Fourier Transform of the surface elevation time series. The xf values are then multiplied by their complex conjugates. The information is normalized per frequency bin as shown in the denominator using the sample rate (rate) and the number of points (n). The frequency axis is then formed by,

$$f = \frac{(\text{rate})(1:n)}{n}. \quad (10)$$

The irregular heave response data sets of the forward and aft end of the floating tube can be analyzed in the same manner as was the surface elevation, creating a one-sided heave response energy density response spectrum, $G_{Heave}(f)$. The same is true for tension response data sets, assuming a linear relationship. Therefore, the one-sided tension response energy density spectrum would be denoted as $G_{Tension}(f)$. Frequency domain heave and tension transfer function calculations are then performed using

$$|H_{Heave}(f)| = \left[\frac{G_{Heave}(f)}{G_\eta(f)} \right]^{1/2} \quad (11)$$

and

$$|H_{Tension}(f)| = \left[\frac{G_{Tension}(f)}{G_\eta(f)} \right]^{1/2}, \quad (12)$$

where units are cm/cm and N/cm, respectively. These transfer functions are then used as the corresponding response amplitude operators which, assuming a linear system, describe the response of the model due to the forcing.

2.2.3 RAO Data Processing

To determine the heave RAO value at a specific frequency, the average standard deviations of the vertical displacements of the model at each end were divided by the average standard deviation of the water surface elevation for that run, according to Eq. (4). The tension RAO values were calculated using the average, standard deviation, or sum of the average and standard deviation of the attachment load divided by the average standard deviation of the water surface elevation for that run, according to Eqs. (5), (6), and (7). The average RAO values of the repeated runs for a set of conditions were plotted against the frequencies of their respective

regular waves. When applicable, the wavelength to model length ratios (L_m/l_m) are shown on the graphs to indicate possible points of interest in the relationship between forcing and response.

The results from the irregular wave tests were analyzed using the spectral analysis technique to determine an RAO curve over a range of frequencies as described in Chakrabarti [12], Bendat and Piersol [13], and Section 2.2.2. Computations using the Fast-Fourier Transform (FFT) function in MATLAB were utilized to reduce the wave and response time series data to the frequency domain with Eqs. (9) and (10). Then, the output spectrum (response) over the input spectrum (wave forcing) yielded the response transfer function (RAO curve) as per Eqs. (11) and (12). The RAO values from the spectral analysis were also bin-averaged with a 16-point band to smooth the results for each condition.

2.3 Uncertainty Analysis

Precision uncertainty estimates for all physical modeling measurements were made through repeatability tests. Six replicate tests were conducted for every situation modeled, except for testing the 6 MIL tube in waves and the fixed-end 3 MIL tube in waves and towing. For each of these investigations, four replicate tests were conducted.

From each test, the required measurements were averaged over a truncated period of desired response. Then, the mean of these values (\bar{X}) was determined using

$$\bar{X} = \frac{1}{N} \sum_{i=1}^N X_i, \quad (13)$$

where N = the number of individual readings X_i . Using the sample mean, the standard deviation (S_x) was calculated as

$$S_x = \left[\frac{1}{N-1} \sum_{i=1}^N (X_i - \bar{X})^2 \right]^{1/2}. \quad (14)$$

The 95% precision confidence limits for each value were then calculated by multiplying the standard error of the mean (SEM),

$$SEM = \frac{S_x}{\sqrt{N}}, \quad (15)$$

by the two-tailed t value associated with the corresponding degrees of freedom, $N - 1$ ($t = 2.571$ for five degrees of freedom (six tests); $t = 3.182$ for three degrees of freedom (four tests)) [14].

When possible, the bias error was determined from the measurement device characteristics and combined with the precision error to yield total error for the measurement according to

$$Error_{Total} = \sqrt{Error_{Precision}^2 + Error_{Bias}^2}. \quad (16)$$

Precision error was calculated for the towing speed and water surface elevation measurements while total error (combined precision and bias) was calculated for the attachment load measurements and for the measurements of front and rear vertical displacement.

3 Physical Modeling Experiments

3.1 Overview

The physical modeling experiments were conducted in the 37-meter long, 2.4-meter wide, and 1.5-meter deep test tank in the Hydromechanics Laboratory at the United States Naval Academy. The tank includes a towing carriage and a flap-type wave maker. A scaled physical model was designed and constructed so it could be attached to the carriage and subjected to waves and currents (towing).

To develop the physical model, the investigation considered a full-scale photobiotic tube to consist of a 15-meter long and 20-centimeter diameter floating plastic tube made of low linear density polyethylene (LLDPE) similar to the concept shown in Figure 1. In the scaling process, both geometric and dynamic similitude characteristics were addressed. The elasticity and flexibility of the plastic was also considered, but it was decided that the majority of dynamic response variations would likely come as a function of tube fill-level rather than material characteristics. The material properties were not a central focus when scale values were determined.

During the scaling process, several aspects of the construction and testing procedures were addressed. First, the model had to be representative of the proposed full-scale geometric design. In addition to matching the dimensions, the analysis had to be comparable to realistic environmental conditions. The test conditions also had to be within the operating parameters of the tow carriage and wave maker. Another major modeling consideration was the availability of construction materials. These four aspects of the project helped define the limits for the scaling process.

One of the first steps was to understand the relationship between the tow and wave-making capabilities in the facility with respect to modeling the environment conditions. The models would need to be tested in towing speeds and wave characteristics that best represented the waves and currents of a possible deployment site. Due to the various potential deployment locations for a floating flexible tube structure, it was decided to perform tow tests at a range of (full scale) speeds between 0.0 m/s to 1.0 m/s.

The characteristics of the towing tank also influenced the model scale. Not only did the smaller models have to fit in the tank, but also enough length was needed to allow ample acceleration and steady speed towing distance with the models. The tank can produce waves at frequencies from 0.4 hertz to 1.4 hertz. Wave heights and wavelengths that are produced in this range had to be compared to potential model sizes so that an effective experimental plan could be developed.

The availability of suitable construction materials was an additional constraint to determine the physical modeling testing protocols and drive the scaling process. It was found that low density polyethylene (LDPE) plastic tubular bags could be purchased in flat rolls at several sizes. This convenience provided multiple scaling options. It was also found that the thickness of the plastic tubes that could be purchased ranged from 1 MIL to 6 MIL. Each roll would yield a certain diameter tube without much degree of flexibility in the size, but the lengths of the tube bags could vary widely according to where they were cut.

3.2 Scaling Approach

3.2.1 Theory

Similitude in a physical modeling context means that a scaled model must have geometric, kinematic, and dynamic similarities to the actual full-sized prototype. Using the

Buckingham-Pi approach, non-dimensional parameters have been developed that are used for comparison between a model and a prototype, depending on which forces dominate. For this project, three of these comparison numbers were considered. Geometric scaling was done with ratios of dimensions such as the length and width. The hydrodynamic similarity of the model and full-sized structure must consider Froude number,

$$Fr = \frac{U}{\sqrt{gl}}, \quad (17)$$

which represents the ratio between inertia and gravity forces, while Reynolds number (Equation 2) represents the ratio between inertia and viscous forces. In Eq. (17), U is the flow velocity, l is the characteristic length, and g is the gravitational constant. In this case, since tests were being performed in waves (and water), the focus was on Froude number scaling, with consideration to the issues associated with Reynolds number. Froude scaling is typical when performing wave tests since gravity is the wave restoring force. Since the tube could be potentially flexible, the structural qualities of the model and full-scale design should have also had similarity. Structural scaling could be done using the Cauchy number,

$$Ca = \frac{\rho U^2}{E_v}, \quad (18)$$

where E_v is the modulus of elasticity and ρ is the density of the fluid. Structural scaling is important if the similarity of the dynamic response of the structure is dominant, but it was hypothesized that the various fill levels in the tubes would have more effect on the dynamic response than would the specific material properties of the plastic bag material. Therefore, the model was designed and constructed to scale with both geometric and Froude number scaling, while taking into account the effects of not scaling with Reynolds number or Cauchy number. The material was chosen to be most representative of what the scaled material might be, rather than exactly matching Cauchy numbers at both scales for model construction.

Froude number scaling was based on the geometric ratio,

$$\lambda = \frac{l_p}{l_m}, \quad (19)$$

where l_p and l_m are the length of the prototype and the length of the model, respectively. This ratio can also be used to scale speeds, forces, accelerations, and pressure, among other parameters. Time and velocity, for example, are scaled according to $\lambda^{1/2}$, and forces are scaled according to λ^3 [12].

3.2.2 Procedure

The scaling procedures were done for the 37-meter testing tank in the Naval Academy's Hydromechanics Laboratory. In general, the approach was to first start with geometric scaling. Since the prototype dimensions were already set, the model length and diameter were determined using the scale ratio. The scale ratio was also used to determine the deployment depth relationship by multiplying the scale times the depth of the testing tank.

The current velocity of the full-scale prototype was determined to range from 0.0 m/s to 1.0 m/s and was represented by a series of eight values. For each actual speed value, various Froude number scales were applied to calculate potential model tow speeds. The resulting scaled model towing speeds were compared to the operational capabilities of each tank towing carriage. Comparisons were also done to investigate the relationship between the model length and towing speed with respect to a suitable towing distance in each tank.

Wave characteristics were also scaled according Froude number relationships. In each of the testing tanks, waves can be produced with periods ranging between 0.7 and 2.5 seconds. Using this range, the wavelengths were calculated from the wave periods according to the depth of each tank following the dispersion relation for linear wave theory,

$$\omega^2 = gktanh(kd), \quad (20)$$

where ω is the wave radian frequency, g is the gravitational constant, k is the wave number, and d is the water depth.

The range of wavelength values was then compared to the model size options at each scale ratio, since wave tests will consider multiples of wavelengths to model lengths. Lastly, using the range of scale ratios, the full-scale wavelengths, deep-water wavelengths (according to Equation (20)), and wave periods were calculated. These values helped to characterize the full-scale environmental conditions of a potential deployment location that each scale modeled. Once the model-scale environmental conditions were determined, an assessment was made concerning the relevancy of potential full-scale deployment sites.

3.2.3 Physical Model Scaling Results

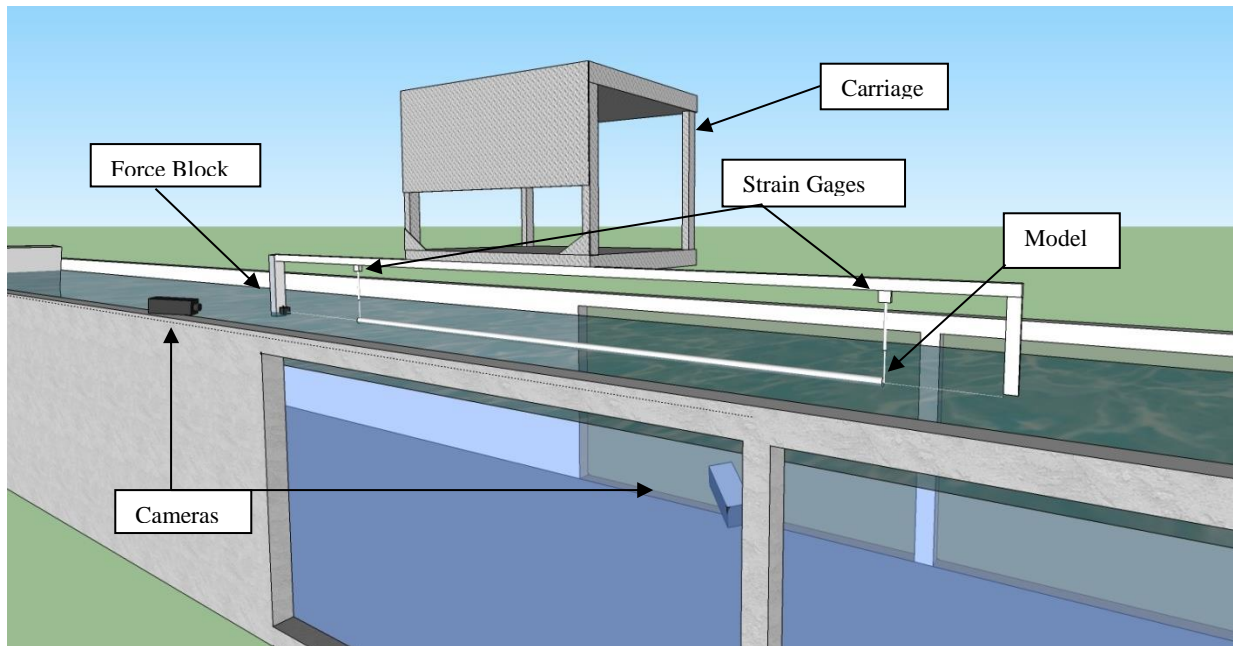
To determine the optimal geometric scale, main considerations were the testing capabilities of the towing tank, the availability of building materials, and the suitability of the modeled full-scale conditions. From a range of possible scaling ratios and the corresponding full-scale conditions, an optimal ratio of 1:4 was selected. The actual scale, however, was determined using the available materials with a value of 1:4.21 chosen. Based on this ratio, the model was built to be 3.62 meters long and 4.83 centimeters in diameter. The full-scale depth would be 6.42 meters and the wave periods could range from 1.47 seconds to 5.13 seconds. The wavelength to model length ratios (Lm/lm) could range from about 0.22 to 2.23 (wavelengths per model length). This range of Lm/lm ratios provided opportunities to test at ratios of wavelength to model length of 0.25, 0.50, 1.0, and 2.0. Table 1 provides a summary of the scaling results for the 37-meter testing tank.

Table 1: 37-meter Testing Tank Scaling Results Summary

Full-Scale Prototype			
Dimensions		Conditions	
Prototype Length (m)	15.2	Current Range (m/s)	0.00 - 1.00
Prototype Diameter (cm)	20.3	Frequency Range (Hz)	0.19 - 0.68
Prototype Depth (m)	6.42	Period Range (s)	1.47 - 5.13
		Wavelength Range (m)	3.36 - 34.06
1:4.21 Scale Model			
Dimensions		Conditions	
Model Length (m)	3.62	Current Range (m/s)	0.00 - 0.50
Model Diameter (cm)	4.83	Frequency Range (Hz)	0.40 - 1.40
Model Depth (m)	1.52	Period Range (s)	0.71 - 2.50
		Wavelength Range (m)	0.80 - 8.09
Wavelength to Model Length Multiple Range			0.22 - 2.23

3.3 Experiment Setup

All experiments were conducted in the 37-meter towing tank facility. The model was attached to the towing carriage as illustrated in Figure 2. Figure 3 shows the model and test apparatus in place in the testing tank.

**Figure 2: 37-meter tank experiment setup**

During the tests, the horizontal load from model resistance was measured using a force block mounted on the forward end of the mount assembly. Water surface elevation was measured using a capacitance wave gage at the front of the model. The vertical displacements at the ends of the model were measured using a combination of strain gages and springs. Cameras above and below the water surface were used to qualitatively analyze the model response during each run.

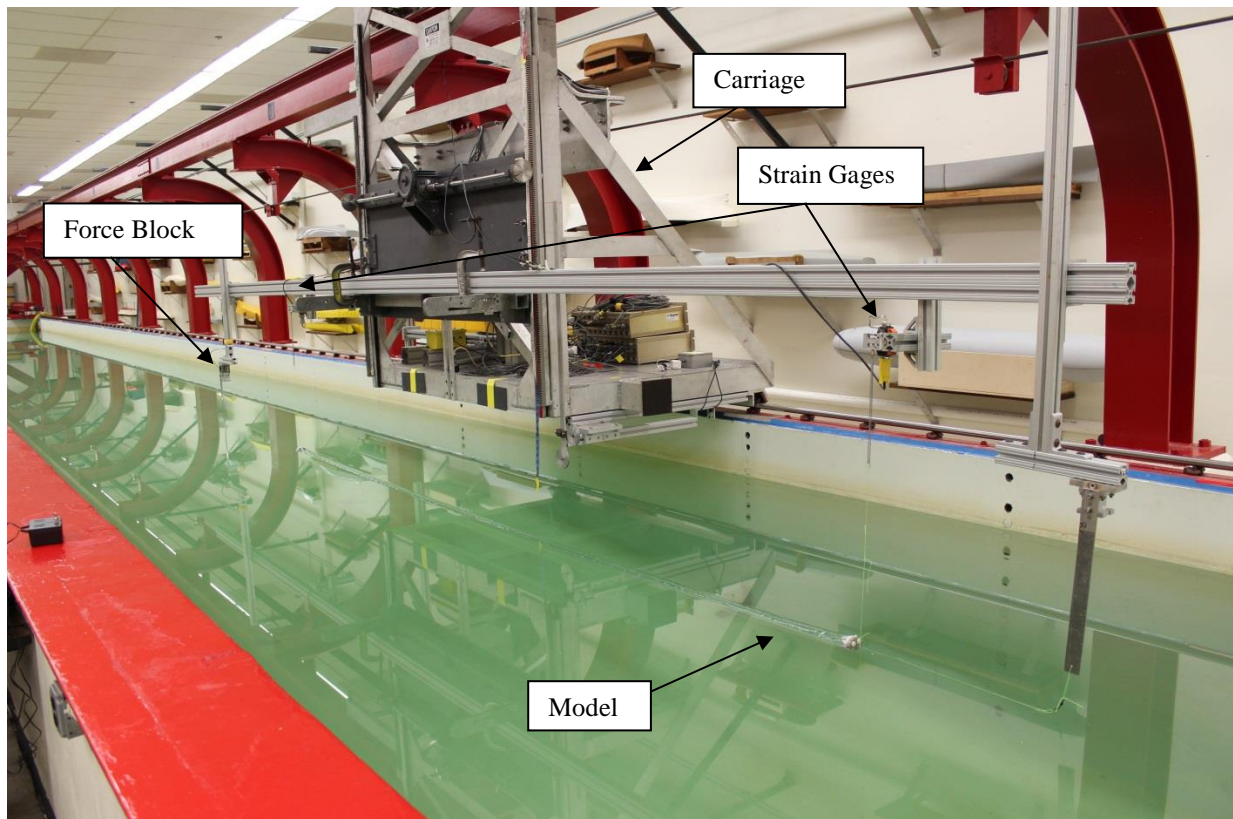


Figure 3: The experiment setup showing the model in the water attached to the force block at the front of the carriage and the strain gages attached to each end cap with a spring and fishing line.

As depicted in Figure 4, each end of the tube ends were sealed with a machined end cap with an eyelet in the center. The tube was attached to the forward and rear struts by the eyelets

on the end caps using fishing line. Vertical displacements (i.e. heave) were measured at each end cap using a calibrated strain gage and spring system.



Figure 4: Tube end caps

Two attachment techniques were utilized in this investigation. For most of the tests, the forward end of the tube was connected to the leading strut via a relatively inelastic length of fishing line. This attachment method allowed the forward end cap freedom to move in the vertical axis. The next attachment method involved a fixed attachment point at the leading end of the tube, as if the tube were connected to an outflow manifold as shown in Figure 1. In this method, the forward end of the tube was fixed directly to the forward strut. Figure 5 shows the free-end attachment method and Figure 6 shows the fixed-end attachment method.

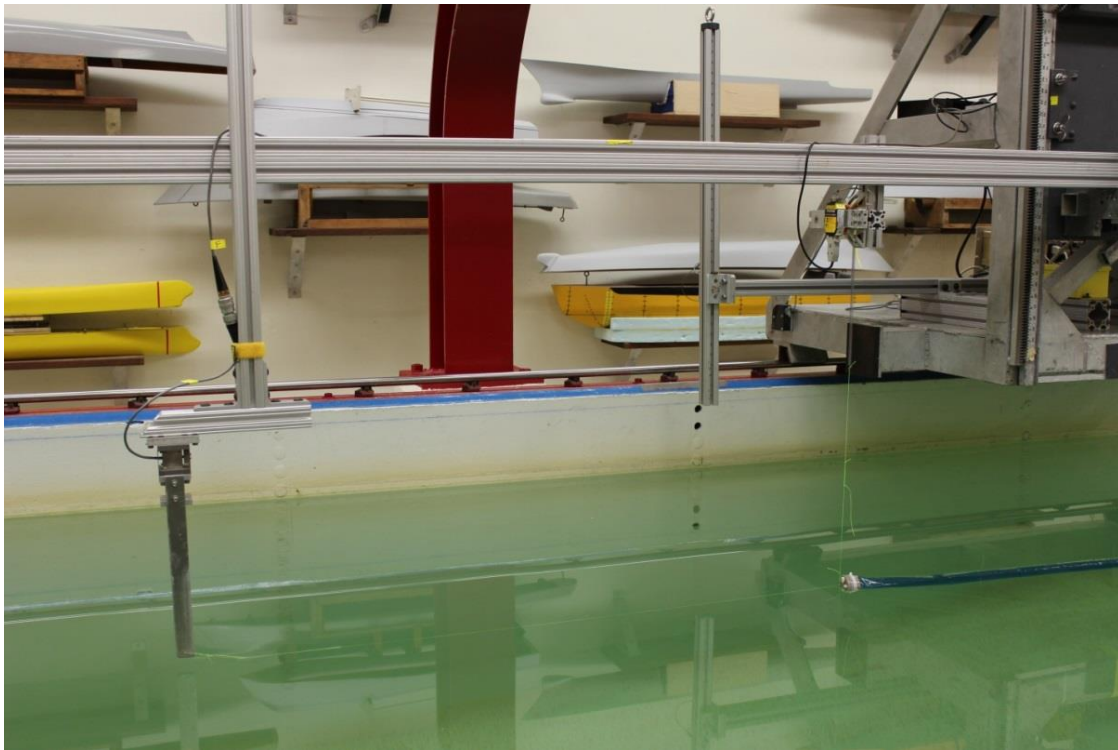


Figure 5: Free-end attachment with the inextensible tow-line.

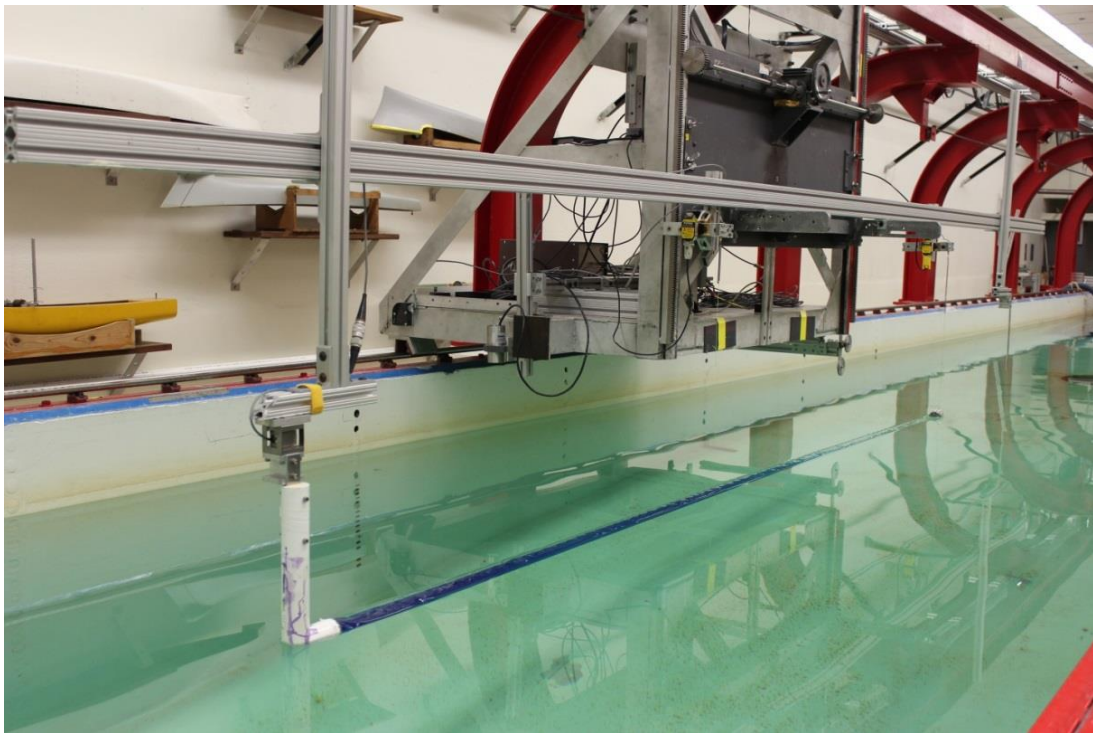


Figure 6: Fixed-end attachment with the tube directly attached to a pipe structure.

3.4 Testing Procedure

For the steady drag tests, the model was towed at speeds from 0.06 m/s to 0.49 m/s to represent full-scale currents with values from 0.12 m/s to 0.98 m/s, respectively. For each set of conditions, the model was towed at the desired speed and the attachment load was measured from the force block. Six tests were performed for each set of conditions. This process was completed with the model at 50% and 95% fill levels. Tests were also conducted with both the leading end of the tube free and fixed to the forward vertical strut.

For the wave tests, the model was tested at the same two fill levels (50% and 95%), and with the two attachment configurations (free- and fixed-end). The wave tests were conducted with steepness values of 1/30. Thirteen regular wave conditions and one irregular wave condition were tested, each with six replicates. The regular wave periods ranged from 0.71 to 2.22 seconds, representing full-scale periods of 1.47 to 4.56 seconds. For comparison to the 3 MIL model, a 6 MIL model was tested in six regular wave conditions (four runs each) and one irregular wave condition (six runs) using the free-end attachment method.

In addition to the regular wave tests, irregular (random) wave testing was also conducted. A JONSWAP spectrum was programmed into the wave maker with a significant wave height of 7.62 centimeters, a dominant period of 1.4 seconds, a shape factor of 3.3, a minimum frequency of 0.3 Hz, and a maximum frequency of 1.5 Hz. Figure 7 shows a plot of the input spectrum.

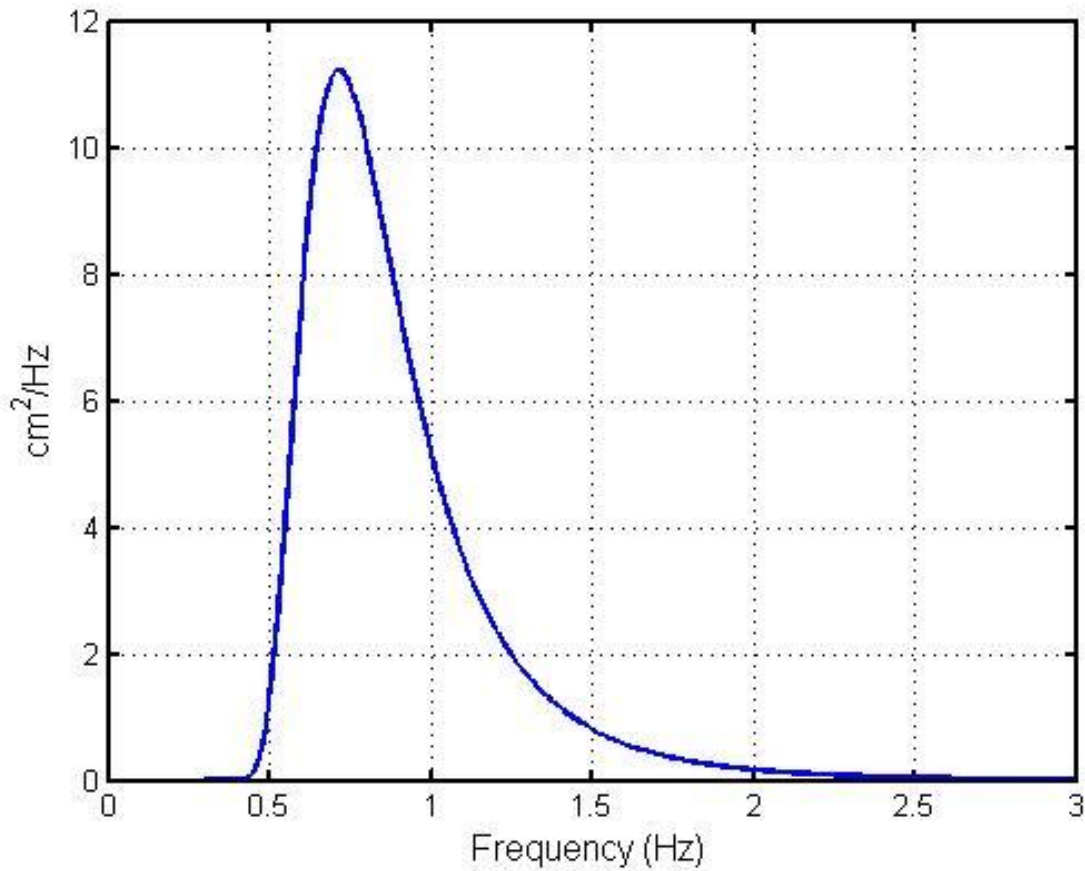


Figure 7: Energy spectral density of JONSWAP irregular wave input spectrum.

For wave and current tests, the 3 MIL model was towed through the tank at speeds of 0.12, 0.30, and 0.49 meters per second and tested in waves with periods of 1.54, 1.05, and 0.77 seconds at each towing speed. Again, the model was tested at 50% and 95% fill levels. Six runs for each condition were completed using the free-end attachment, and four runs for each condition were completed using the fixed-end attachment.

4 Computational Fluid Dynamics

Computational Fluid Dynamics (CFD) analyses were conducted in conjunction with the physical model tests. CFD simulations were performed considering a model of the tube at 100% full and 50% full. In the CFD software, the 100% full tube was modeled as a solid circular cylinder 3.62 meters long and 4.83 centimeters in diameter. An elliptical cross-sectional shape represented the 50% full tube. The surface area of elliptical shape was kept equal to that of the circular cylinder, while major and minor axes were adjusted to represent the tube at a lower fill level, assuming little or no stretch in the material. Previous research on the shape of flexible tubes at various fill levels was used to help determine the specific shape of the tube when 50% full [15]. The 50% full tube was modeled as an elliptical cylinder at 3.62 meters long, 3.08 centimeters high, and 14.33 centimeters wide. Figures 8 and 9 show the solid models of the 100% and 50% full tubes, respectively.

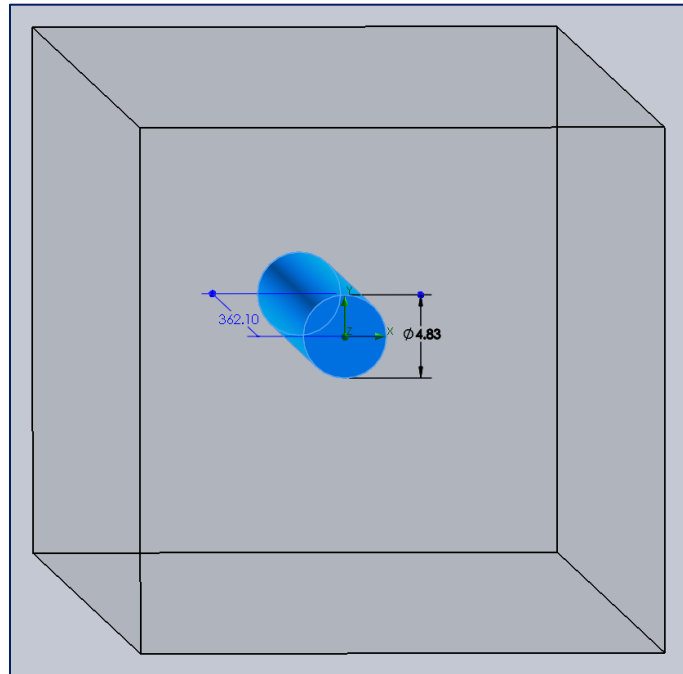


Figure 8: CFD Model of 100% Full Tube

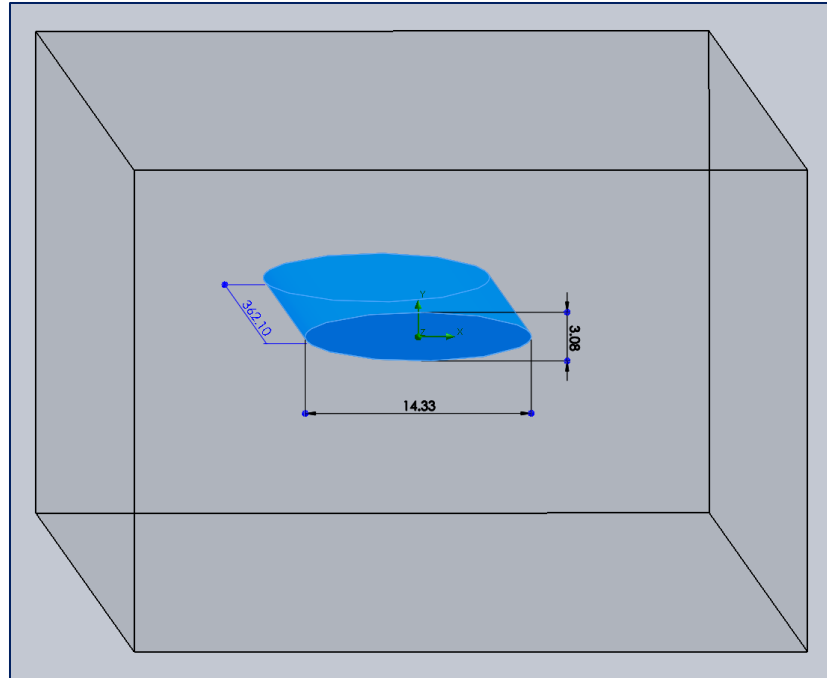


Figure 9: CFD Model of 50% Full Tube

In the CFD software, both tube models were subjected to uniform and parallel flow at eight velocities from 0.06 m/s to 0.49 m/s to match the physical model tests. The computational volume for the 100% full model was a rectangular prism that was 8.53 meters long, 0.30 meters wide, and 0.30 meters tall. The front end of the tube began about 0.34 meters into the volume and the volume extended past the rear end of the tube about 4.57 meters. The computational volume for the 50% full model was a rectangular prism that was 8.53 meters long, 0.43 meters wide, and 0.30 meters tall. The front end of the tube began about 0.34 meters into the volume and the volume extended past the rear end of the tube about 4.57 meters.

The CFD code associated with the SolidWorks Flow Simulation tool was applied for this application. Flow Simulation uses the finite volume method on a “spatially rectangular computational mesh designed in the Cartesian coordinate system with the planes orthogonal to its axes and refined locally at the solid/fluid interface” to solve the Navier-Stokes governing

equations. Specifically, the code applies the Favre-averaged Navier-Stokes equations and the k- ϵ turbulence closure technique so that the system differential equation can be solved numerically for turbulent flow conditions. [16]

Figure 10 shows the computational mesh and velocity flow field of the tube modeled as 100% full and Figure 11 shows the computational mesh and velocity flow field for the tube model representing the tube at 50% full. In both images, a view from each perspective is provided. For each model configuration, the CFD software calculated the forces on the tubes as if they were fully submerged.

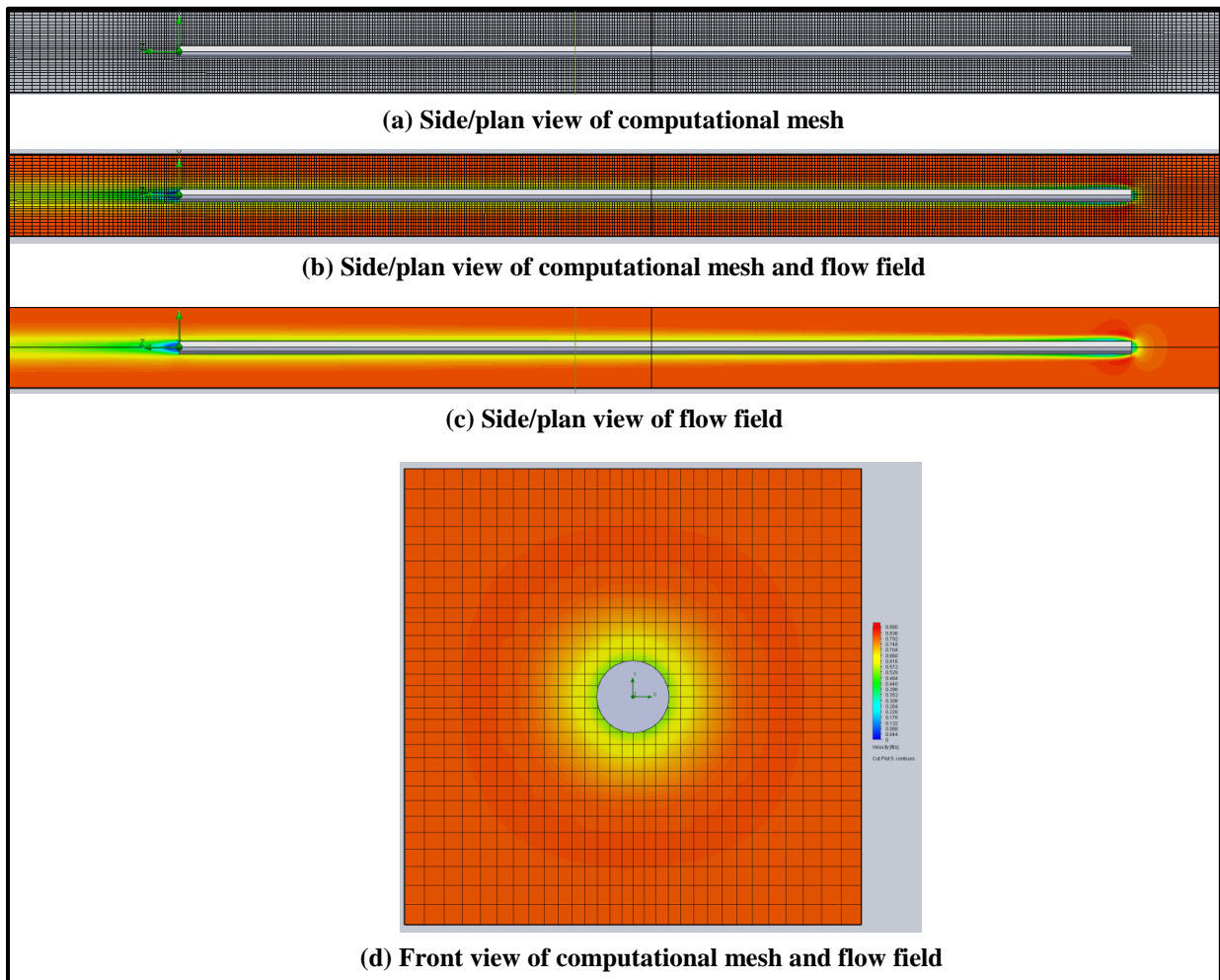


Figure 10: Computational Mesh and Flow Field for 100% Full CFD Model

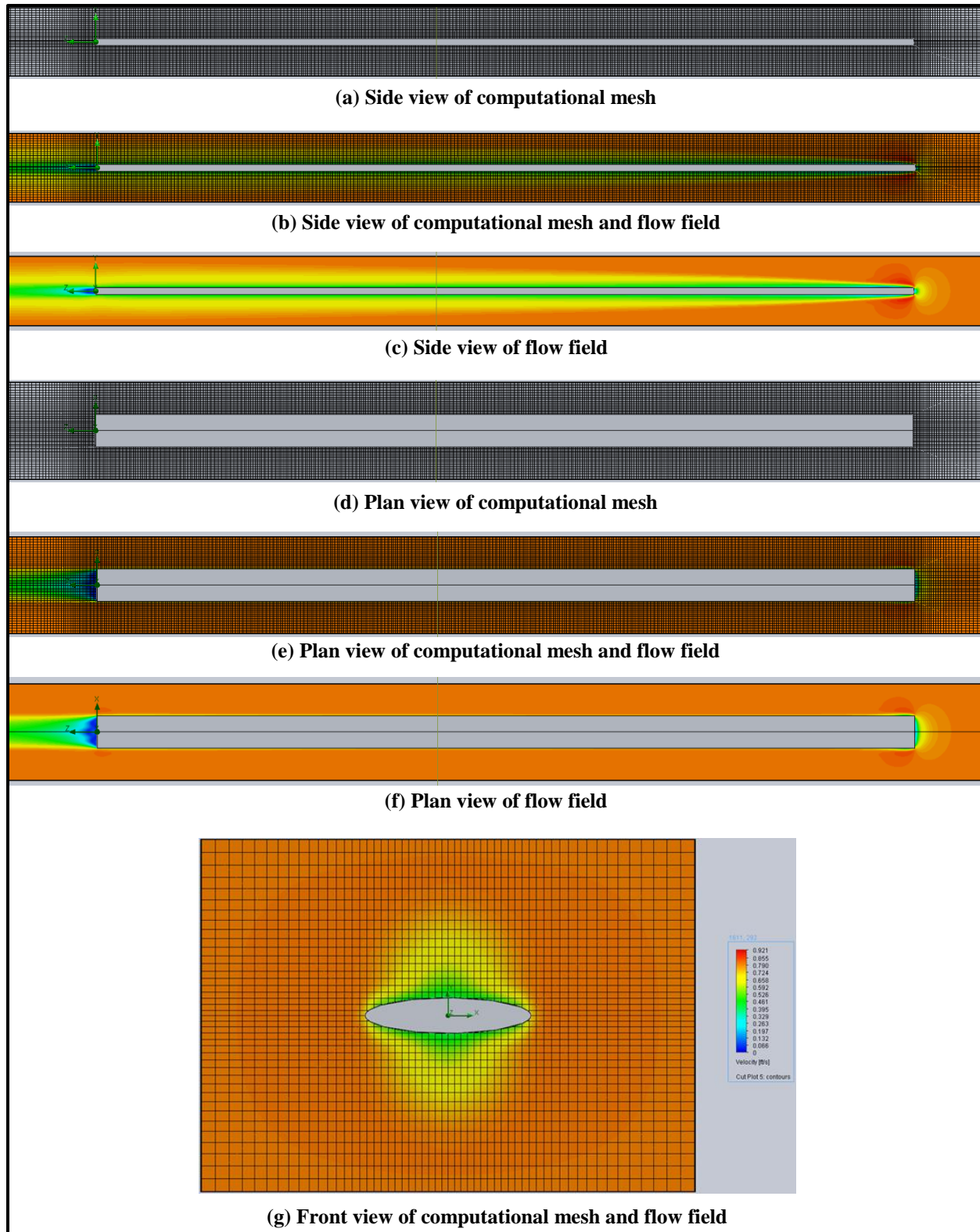


Figure 11: Computational Mesh and Flow Field for 50% Full CFD Model

5 Results and Discussion

5.1 Model and Simulation Results in Currents

As described in Section 2.1, CFD simulations were performed at a range of Reynolds number values to investigate the flow field characteristics related to the drag coefficient (C_D). The simulations were conducted using the 100% full model with Reynolds numbers ranging from 10 to 10^7 . The C_D values at each Reynolds number were calculated according to Eq. (1) and plotted on a log-log plot against reference C_D values from Hoerner [11]. Figure 12 shows the results.

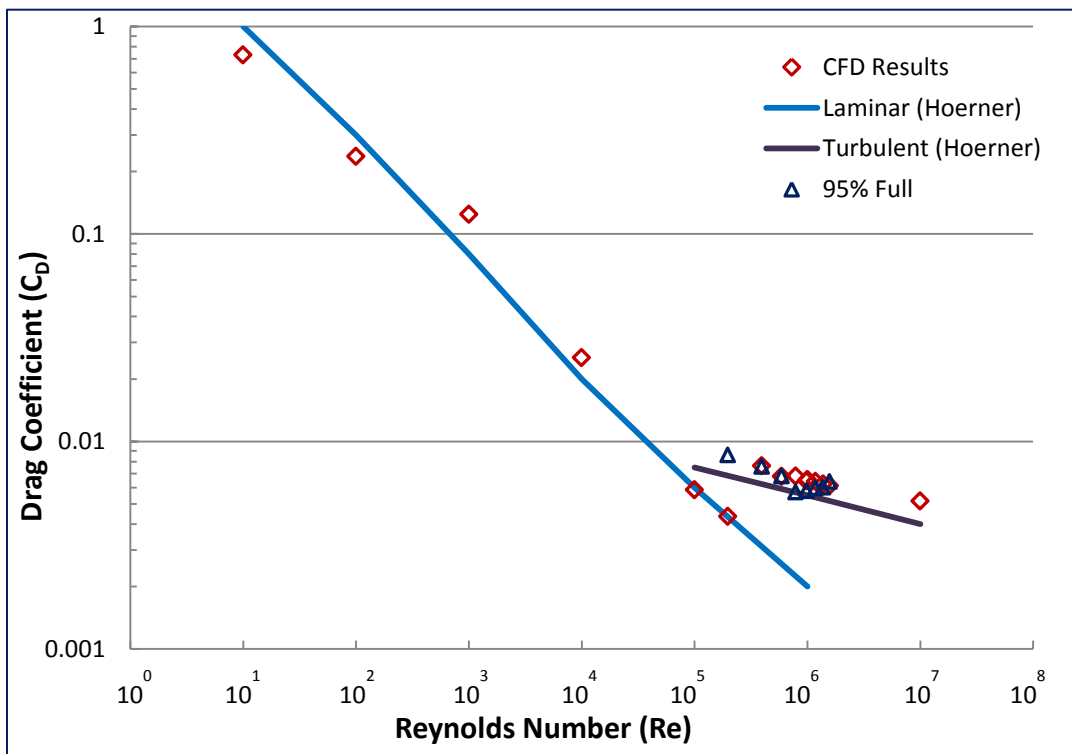


Figure 12: Drag coefficients from CFD simulations and Hoerner [11] across a range of Reynolds numbers from $Re=10$ to $Re=10^7$.

The results from the CFD simulations show that the C_D value decreases steadily with increasing Reynolds numbers, but the trend changes in Reynolds numbers above 10^5 . From the information on Figure 12, it appears that a transition from laminar to turbulent flow occurs at a

Reynolds number of approximately 10^5 . The results from the physical modeling also indicate turbulent flow, which reduces drag coefficient dependency on Reynolds number. To use the above information in the design process, drag coefficients could be directly obtained from the non-dimensional Reynolds number regardless of scale and applied with Eq. (1).

5.2 Free-End Attachment

5.2.1 Drag Tests

The next set of results (Figure 13) shows the force values for the free-end attachment model towed at speeds from 0.06 m/s to 0.49 m/s at the two fill levels (50% and 95%). Six replicates were obtained for each tow speed. Figure 13 also shows the corresponding CFD results for the 50% and 100% solid models.

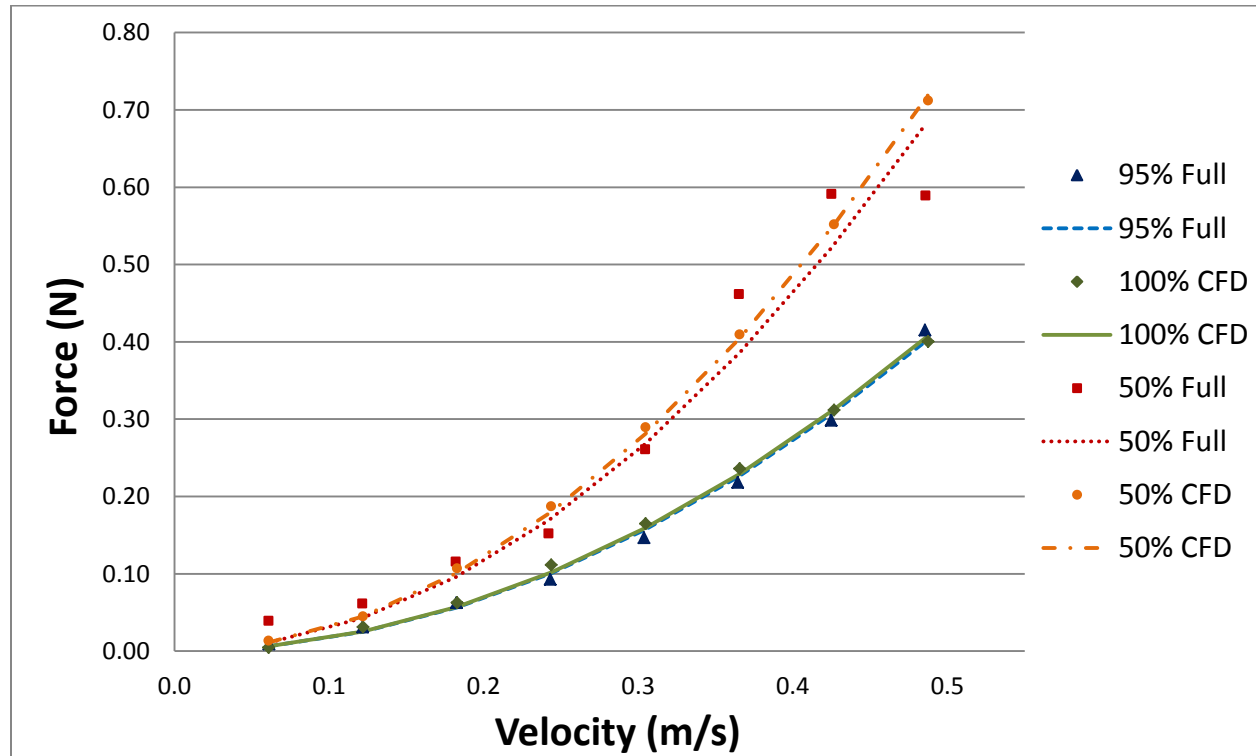


Figure 13: Free-end drag test results from both the physical model tests and CFD. The dotted and solid lines are the curve fit values of the individual tests (points) in the series.

Using the curve fitting approach from Eqs. (1) and (3), the C_D for this model was calculated for each test series. In Eq. (1), 999.8 kg/m^3 was input for ρ and the wetted surface area of the tube (0.549 m^2) was input as the reference area, A . The 50% and 95% full physical model test results produced C_D values of 0.010519 and 0.006184, respectively. Using the same technique, the CFD simulations of 50% and 100% full cylinders yielded C_D values of 0.011030 and 0.006254, respectively.

Overall, both the 50% and 95% full average experimental drag forces and calculated C_D values compare well to those from the CFD simulations (1.1% error and 4.6% error, respectively). However, random and systematic uncertainty was likely due to the small magnitude of the measured force values. Both the 50% and 95% full tests indicate an average of about 60% total error within the range of tests. Higher uncertainty is observed at the lower tow speeds, but the lowest total uncertainty values still range from 10% to 20% at the higher speeds. Conversely, the average velocity measurements indicate an average random uncertainty of less than 0.25%.

5.2.2 *Wave Tests, 3MIL Model*

At each fill level, the physical model was tested in thirteen regular wave conditions and in irregular waves, each with six replicates. RAO values were calculated according to the procedure described in Section 2.2. Figure 14 shows the results from the regular and irregular wave tests with the model 50% full, and Figure 15 shows the results from the regular and irregular wave tests with the model 95% full. In each of the figures, the solid line and the circle points represent the response of the forward end cap and the dashed line and asterisks represent the response of the rear end cap of the model.

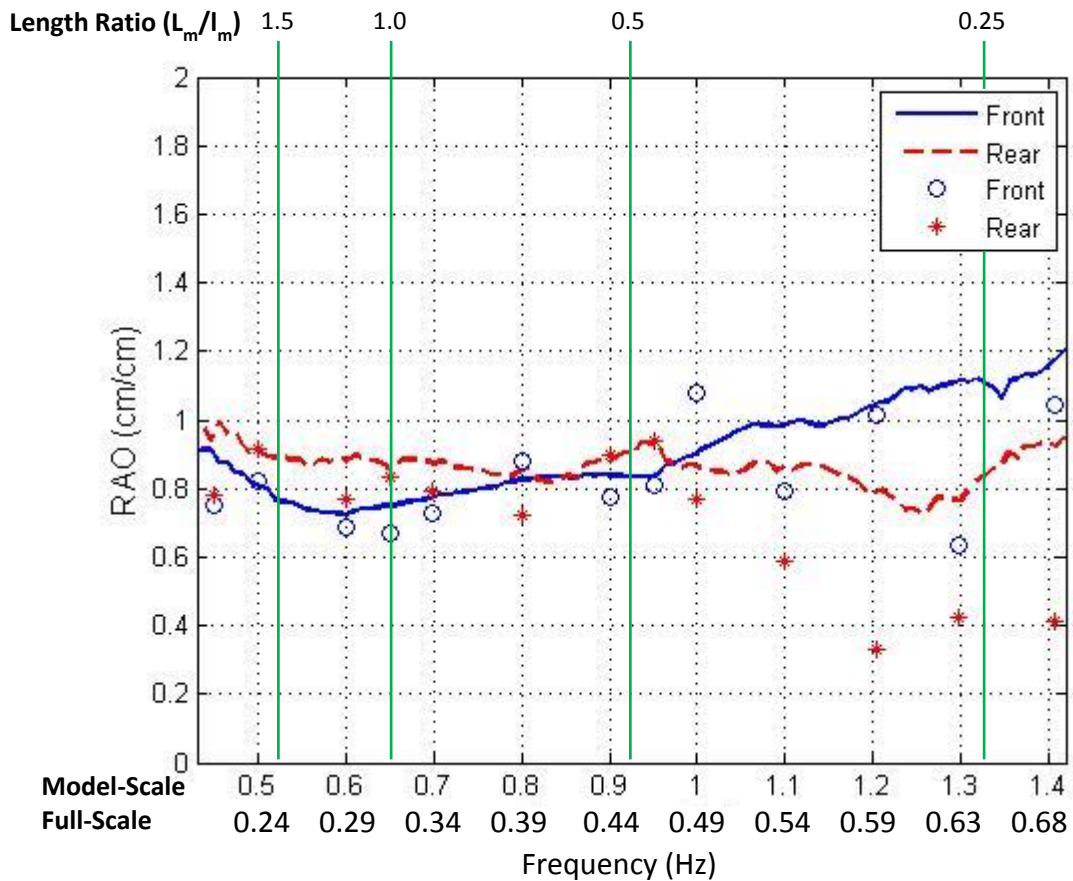


Figure 14: Free-end 3 MIL model response in waves (50% full). The solid line and the circle points represent the response of the forward end cap in irregular and regular waves, respectively. The dashed line and asterisks represent the response of the rear end cap in irregular and regular waves, respectively.

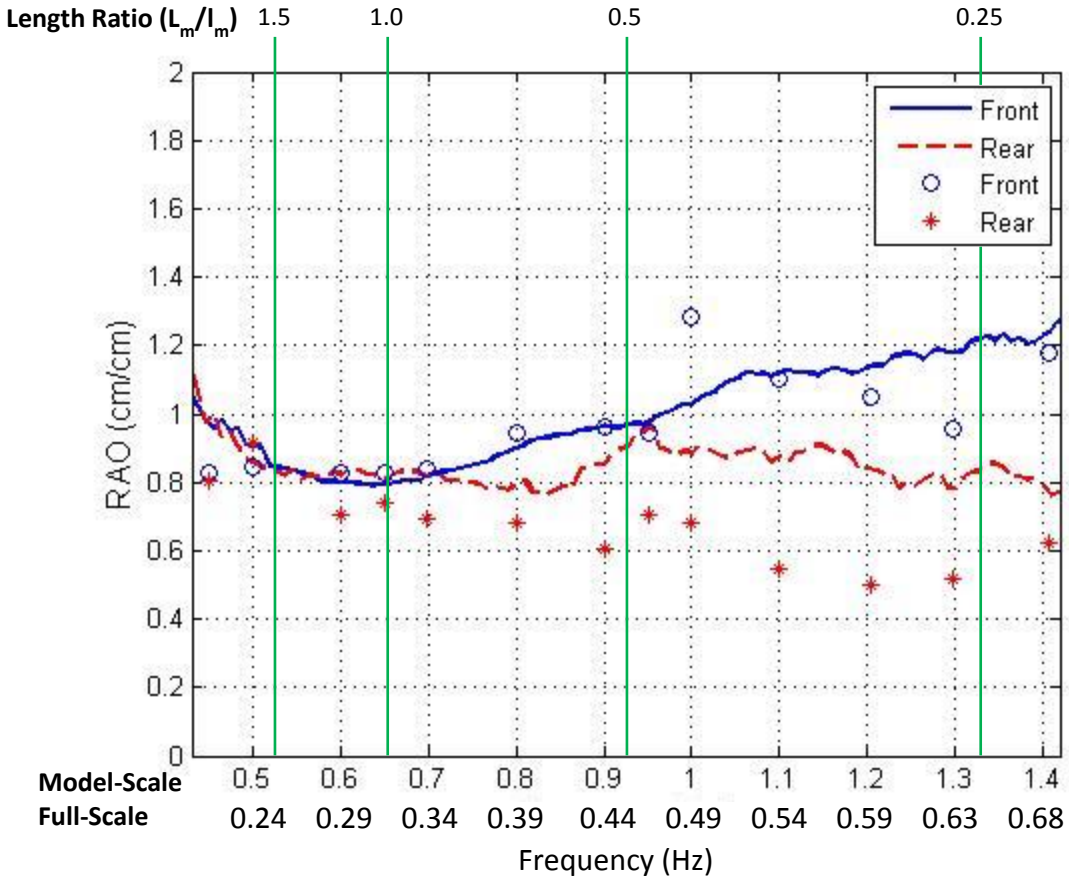


Figure 15: Free-end 3 MIL model response in waves (95% full). The solid line and the circle points represent the response of the forward end cap in irregular and regular waves, respectively. The dashed line and asterisks represent the response of the rear end cap in irregular and regular waves, respectively.

The spectral RAO data sets indicate that the model response tended to follow the wave forcing more at wave frequencies between 0.40 and 0.50 Hz full-scale. For both fill levels, the normalized response of the forward end of the model increased as the wave frequency increased while the response of the rear end of the model remained mostly within an RAO of 0.8 to 1.0 throughout the range of wave frequencies. For the 95% fill level, the forward end of the model tended to exhibit an equal or larger response than the rear end of the model. At 50% full, the front end of the model exhibited a higher response at higher frequencies and the rear end of the model exhibited the higher response at the lower frequencies. At 95% full, the responses of the

front and rear end caps were similar at frequencies below 0.34 Hz full-scale. At higher frequencies, the front end cap response exhibited a response with a RAO greater than 1. The rear end cap, however, shows response RAO values of about 0.8 and 0.9. The results were similar for the model at 50% full, although the separation of the responses occurs at about 0.49 Hz (full-scale). At the higher frequencies, the front end cap also showed a more energetic response with RAO values greater than one, while the rear end cap, once again, exhibited decrease response with RAO values generally less than 1.

Also provided in Figures 14 and 15 are the wavelength to model length ratios (L_m/l_m) with respect to the RAO frequencies. The plots show that at frequencies when the wavelength was $\frac{1}{2}$ that of the model, the front end cap RAO values are greater than 1 for the irregular wave tests. In regular waves, a slight increase in the response of the rear end cap is noticeable at ratios of 0.5, 1.0, and 1.5.

Snap loads from the forward attachment could have contributed to the higher response at the front of the model. Figure 16 shows the attachment loads on the model at 95% full over a series of irregular waves. For these tests, the model was attached to a forward strut and force block using approximately a meter of low-stretch line. Since the line was not stiff, the line exhibited a “snapping” behavior.

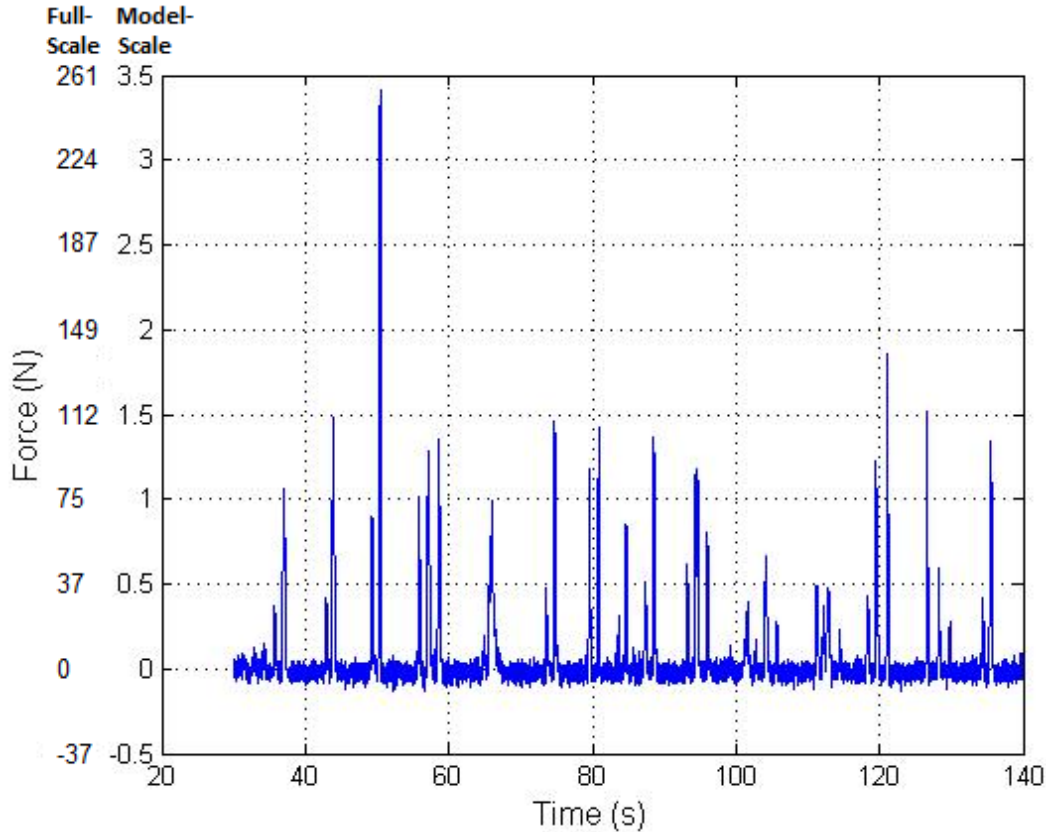


Figure 16: Free-end attachment loads on 95% full model in irregular waves.

The snapping of the line likely caused the increases in attachment load at various instances throughout the wave series. Such snapping could have affected the vertical response at the front end cap more than at the rear end cap, leading to the response differences between the two. The full scale values shown on Figure 16, with a maximum approaching 261 N, will have substantial design implications if a system like this is engineered to become operational.

The attachment loads were also measured throughout the testing. In Figure 17 and 18, the results are presented as RAO values according to Eqs. (5), (6), and (7) in Section 2.2 for the model when 50% full and 95% full, respectively.

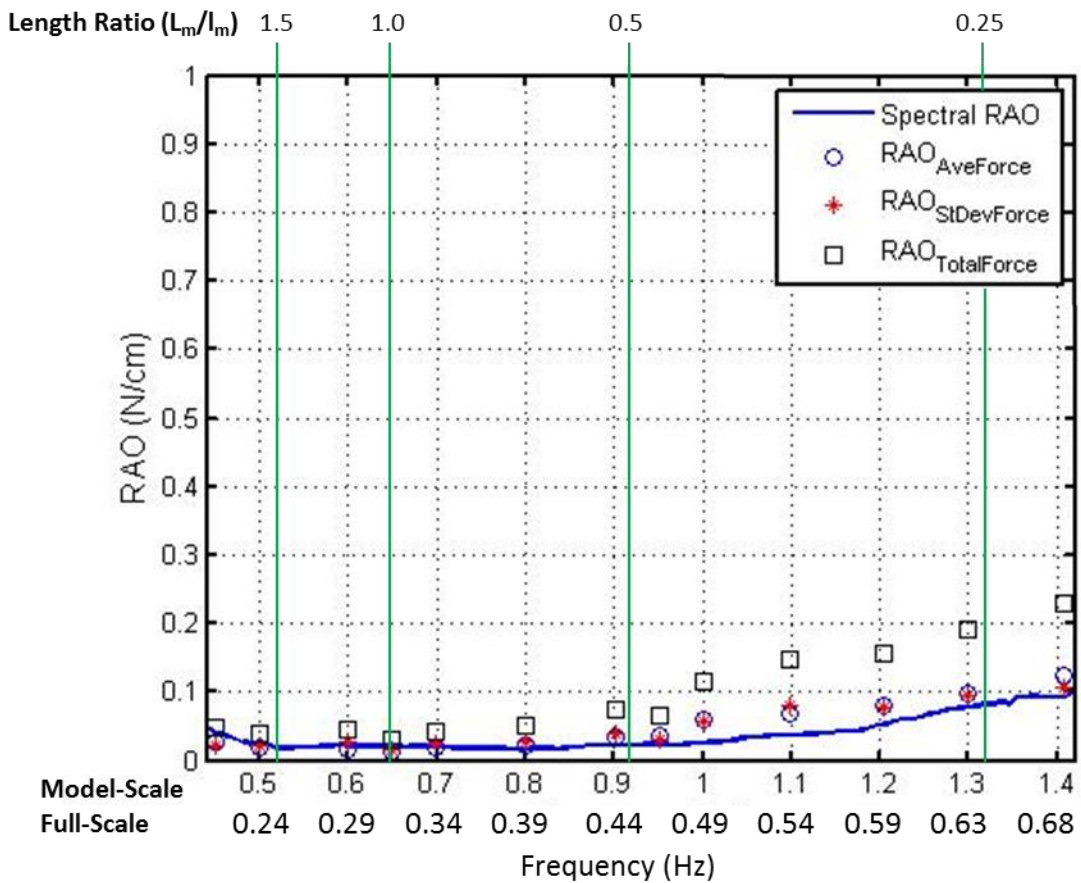


Figure 17: Free-end 3 MIL model response in waves (50% full). The solid line represents the spectral tension RAO. The circle points represent the average tension RAO, the asterisks represent the standard deviation RAO, and the square points represent the sum of the previous two values.

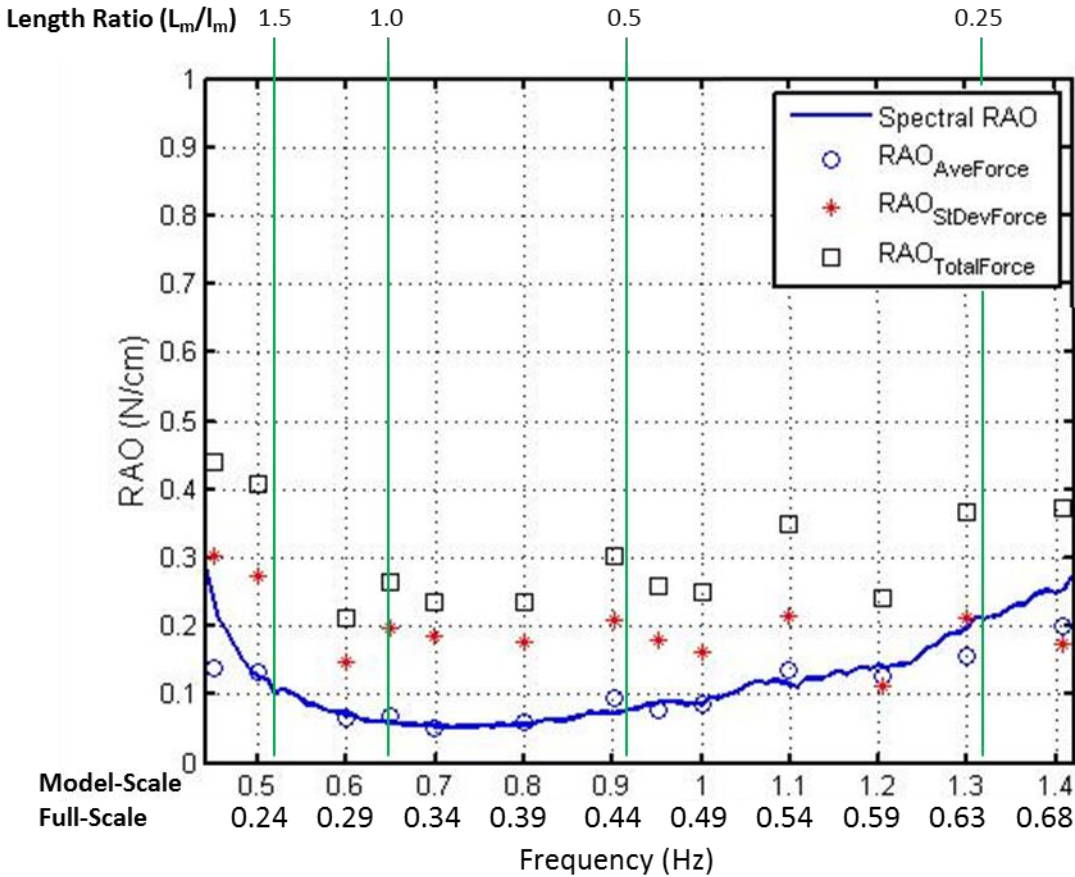


Figure 18: Free-end 3 MIL model response in waves (95% full). The solid line represents the spectral tension RAO. The circle points represent the average tension RAO, the asterisks represent the standard deviation RAO, and the square points represent the sum of the previous two values.

In Figures 17 and 18, the spectral tension RAO tended to follow the RAO points that correlate to average force normalized by wave amplitude. The graphs also indicate that there was higher tension at the model attachment point at both fill levels (50% and 95%) when the wave frequency increased.

Because each test was performed six times, uncertainty values for each measurement could be calculated as described in Section 2.3. Table 2 provides the error percentages for each measurement during testing at each fill level.

Table 2: Measurement error for 3 MIL model with free-end attachment in waves

Fill Level	Wave Forcing	Percent Error (%)			
		Average Tension	Tension Standard Deviation	Forward Response	Rear Response
50%	6.8	68.7	64.6	15.8	16.5
95%	4.5	46.9	36.4	13.4	28.2

5.2.3 Wave Tests, 6MIL Model

The 6 MIL model was tested in the same configurations as the 3 MIL model but in fewer conditions. At both fill levels, the 6 MIL physical model was tested in six regular wave and the single irregular wave conditions. Four replicates were obtained for each of regular wave condition and six replicates for the test in irregular waves. Figure 19 shows the results from the regular and irregular wave tests with the model 50% full, and Figure 20 shows the results from the regular and irregular wave tests with the model at 95% full. In each of the Figures, the solid line and the circle points represent the response of the forward end cap and the dashed line and asterisks represent the response of the rear end cap of the model.

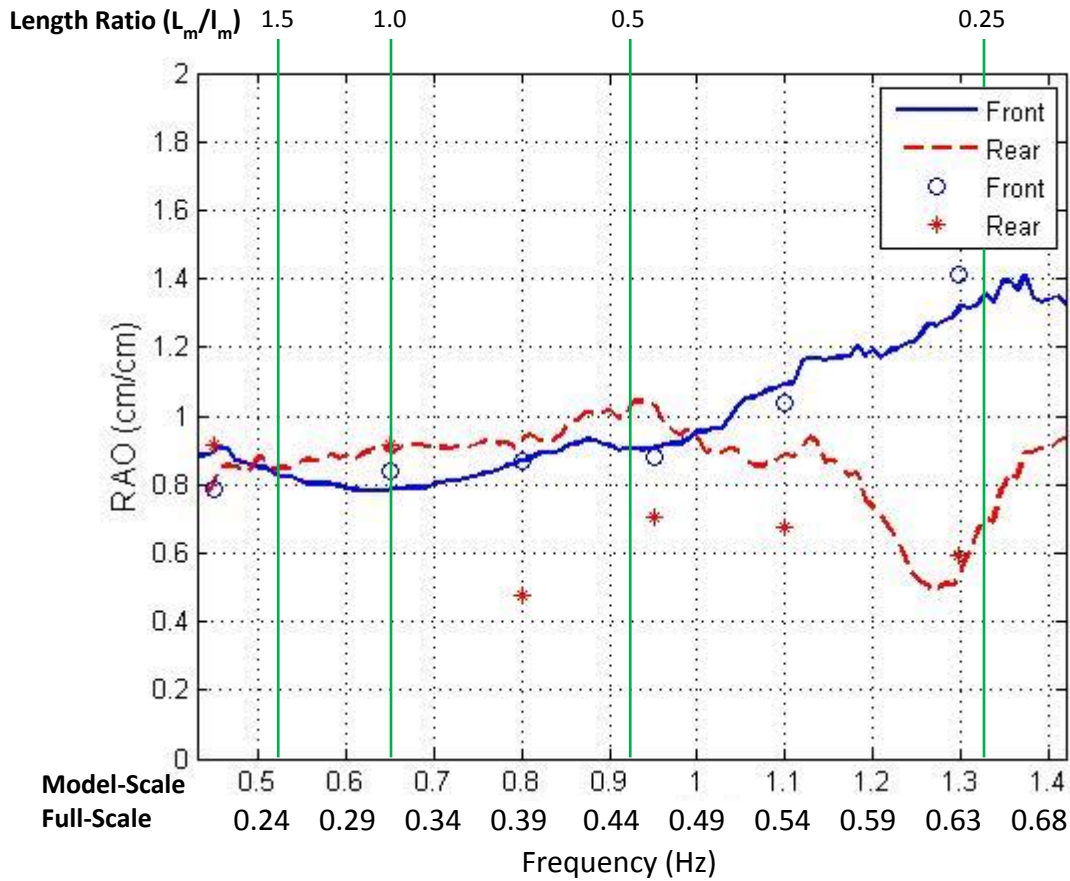


Figure 19: Free-end 6 MIL model response in waves (50% full). The solid line and the circle points represent the response of the forward end cap in irregular and regular waves, respectively. The dashed line and asterisks represent the response of the rear end cap in irregular and regular waves, respectively.

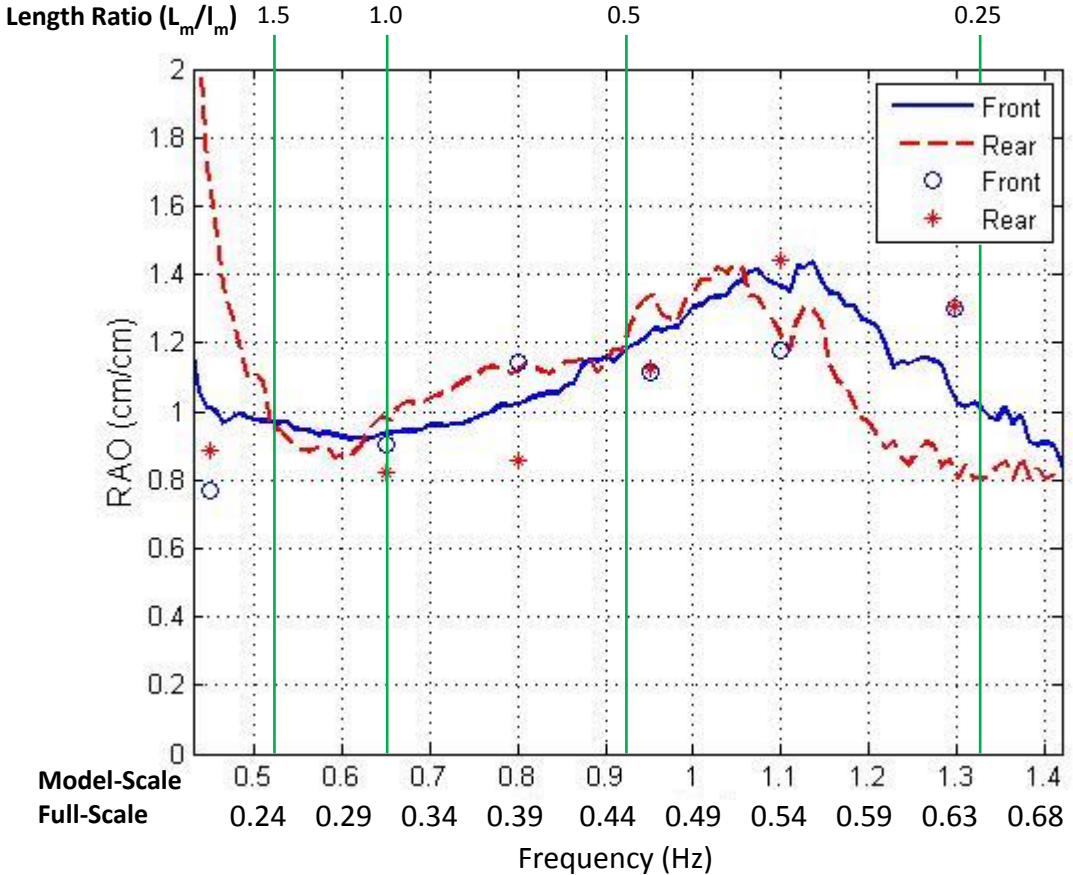


Figure 20: Free-end 6 MIL model response in waves (95% full). The solid line and the circle points represent the response of the forward end cap in irregular and regular waves, respectively. The dashed line and asterisks represent the response of the rear end cap in irregular and regular waves, respectively.

Both graphs show unique differences from the response values of the 3 MIL models. The 6 MIL models generally experience greater responses across the spectrum, though the general trends remain. The response in lower-frequency waves is still less than that in higher frequency waves, and the response from the 95% full model is still higher than that of the 50% model. With the 50% full model, the response of both ends increases with wave frequency, until the response of the rear end cap starts dropping off at about 0.45 Hz (full-scale), or a wavelength to model length ratio of 1. In the results from the 95% full model, it is notable that the responses of both ends are similar and they both peak in waves with a full-scale frequency of about 0.54 Hz.

As with the 3 MIL model, the attachment loads were also measured throughout the testing. In Figure 21 and 22, the results are presented as RAO values according to Eqs. (5), (6), and (7) in Section 2.2 for the model when 50% full and 95% full, respectively.

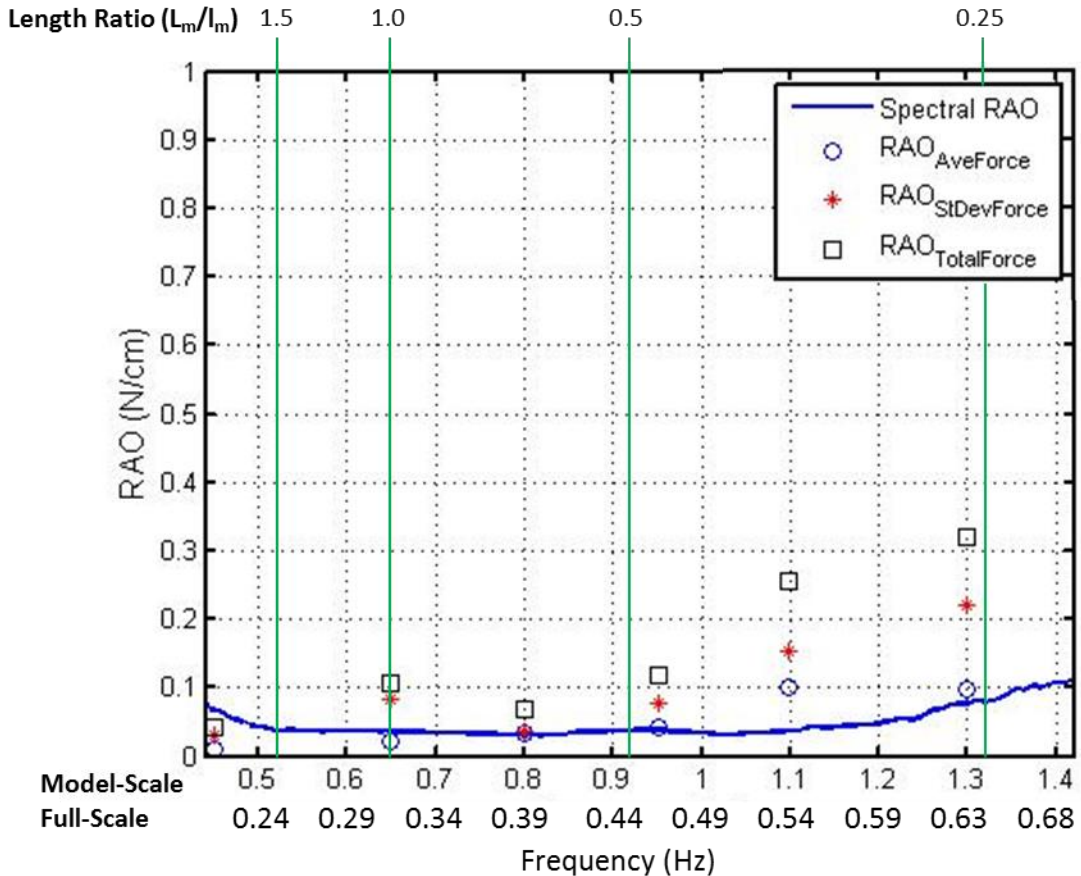


Figure 21: Free-end 6 MIL model response in waves (50% full). The solid line represents the spectral tension RAO. The circle points represent the average tension RAO, the asterisks represent the standard deviation RAO, and the square points represent the sum of the previous two values.

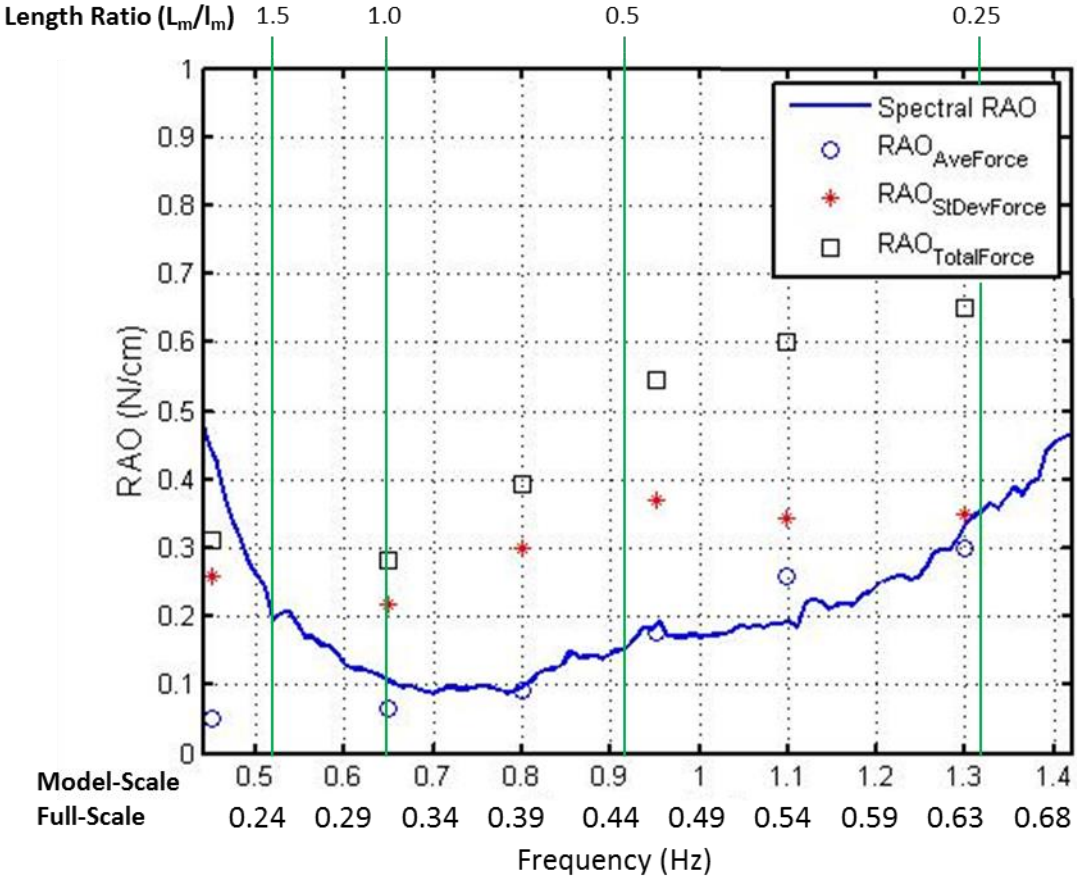


Figure 22: Free-end 6 MIL model response in waves (95% full). The solid line represents the spectral tension RAO. The circle points represent the average tension RAO, the asterisks represent the standard deviation RAO, and the square points represent the sum of the previous two values.

In Figures 21 and 22, the spectral tension RAO tended to follow the RAO points that correlate to average force normalized by wave amplitude, similar to the 3 MIL model. The graphs also indicate that there was notably higher tension at the model attachment point with the model filled to 95% rather than 50%. Both graphs also illustrate an increase in force response at higher wave frequencies, though the trend is much more notable at the 95% fill level. The 50% fill level yielded much more consistent forcing across the spectrum of wave frequencies.

For this series of tests, each set of regular conditions was tested four times and the irregular wave conditions were tested six times. Uncertainty values for each measurement could again be

calculated as described in Section 2.3. Table 3 provides the error percentages for each measurement during testing at each fill level.

Table 3: Measurement error for 6 MIL model with free-end attachment in waves

Fill Level	Wave Forcing	Percent Error (%)			
		Average Tension	Tension Standard Deviation	Forward Response	Rear Response
50%	4.9	59.1	40.8	6.4	8.9
95%	4.6	30.2	28.3	7.6	7.4

5.2.4 Waves and Current Tests

To investigate the response of the model in a combination with both waves and current, the model at two fill levels (50% and 95% full) was towed at 0.12, 0.30, and 0.49 m/s in three sets of regular waves (0.65, 0.95, and 1.30 Hz). RAO values were calculated as described Section 2.2. Figure 23 shows the RAO values of the wave and current tests compared to the RAO values from the wave only tests. The different symbols for the wave and current tests denote the different groups of currents.

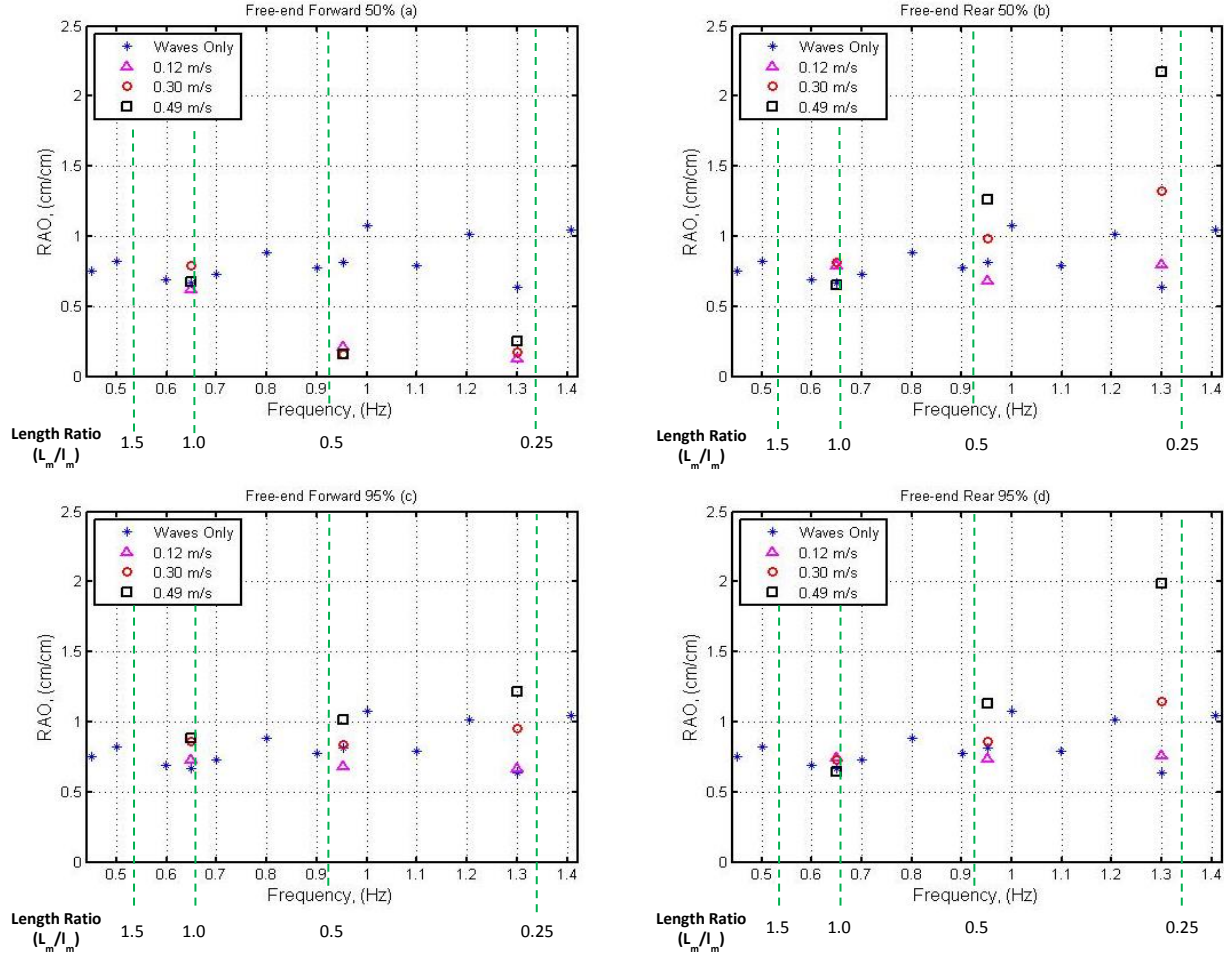


Figure 23: Wave only RAOs v. wave and current RAOs. Each graph presents the same sets of wave/current conditions. The top graphs show 50% full (a, b) and the bottom show 95% full (c, d). The left graphs (a, c) show the front end cap response and the right graphs (b, d) show the rear end cap response. The three symbols stacked at the same frequency represent three different current speeds (0.12, 0.30, and 0.49 m/s) tested with waves of that particular frequency. The asterisks represent tests of waves only.

The addition of a current in waves did not have a significant effect on the response of the forward end of the model. However, in waves with higher frequencies the addition of a current yielded a larger response at the rear end of the model. Additionally, at both end caps, the addition of higher currents yielded higher responses.

In addition to affecting heave response, test results in wave and currents to could influence attachment loads. Figure 24 shows the attachment loads on the model filled to 50% (a) and 95% (b).

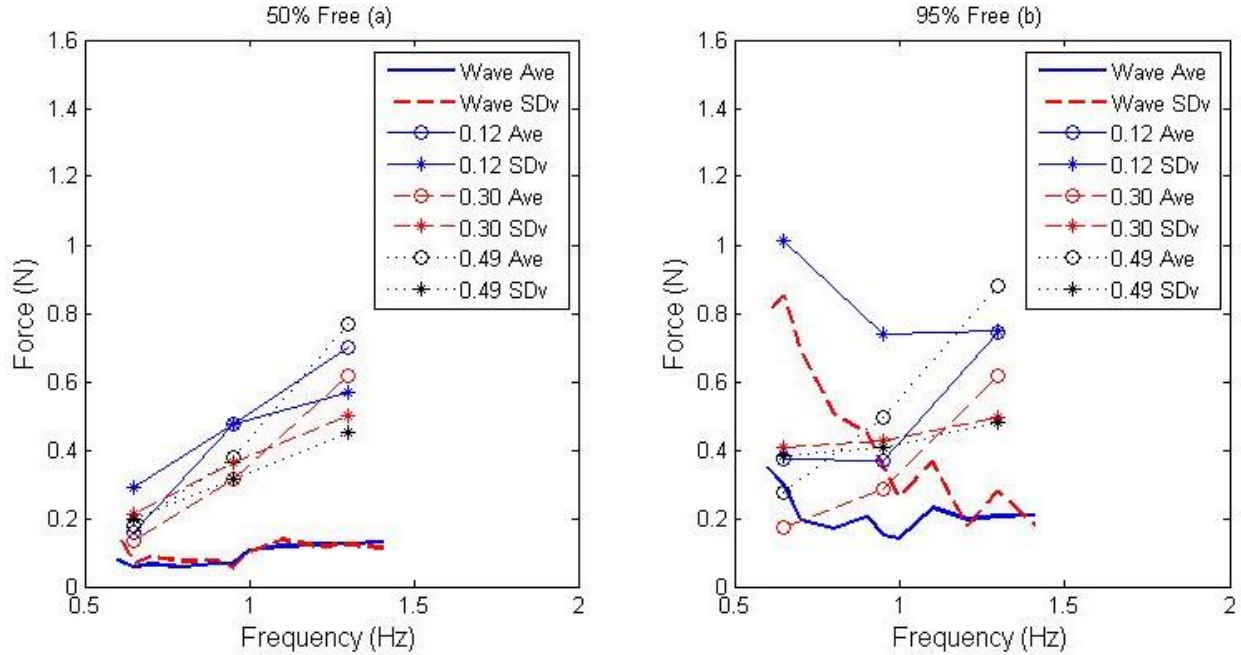


Figure 24: Attachment loads on free-end model filled to 50% and 95% in waves only (thick lines) and waves and current (thin lines). The circle points represent the average load and the asterisk points represent the standard deviation of the load measurements for each current velocity.

The thick lines represent the loads from tests in waves only. The thick solid line represents the average of the attachment loads and the thick dashed line represents the standard deviation of the attachment loads. Typically, the tests in waves yielded lower attachment loads than the test results in waves and current. On each plot, the points connected with thin lines represent the tests of waves and currents. The circle points represent the average of the loads and the asterisk points represent the standard deviation of the loads. The points connected with a thin solid line represent wave tests with an added 0.12 m/s current, the points connected with a thin

dashed line represent wave tests with an added 0.30 m/s current, and the points connected with a thin dotted line represent wave tests with an added 0.49 m/s current.

Overall, the tests indicate that the average attachment loads were typically higher when the model was tested in waves and current than in waves only. In these cases, the water particle velocities associated with the wave likely contributed to the drag on the model. The attachment loads also tended to be higher in waves and currents at higher wave frequencies. It was noticeable that at lower wave frequencies, the standard deviation of the load (likely the force due to the waves) typically dominated the total load. At the higher frequencies however, the opposite was evident as the average of the load was often larger than the standard deviation. This indicates that the steady towing forces are higher than those associated with the higher frequency waves. Lastly, the attachment loads were typically higher on the 95% full model. This was likely due to increased rigidity compared to the model at 50% full.

As in the 3 MIL wave testing, each set conditions was tested six times. Uncertainty values for each measurement could be calculated as described in Section 2.3. Table 4 provides the error percentages for each measurement during testing at each fill level. The large error in the forward response for the 50% full model came mostly from the higher frequency waves and the measurements yielded very low RAOs in that range.

Table 4: Measurement error for 3 MIL model with free-end attachment in waves and currents

Fill Level	Wave Forcing	Percent Error (%)			
		Average Tension	Tension Standard Deviation	Forward Response	Rear Response
50%	3.9	24.0	18.9	159	6.4
95%	3.8	28.2	27.1	18.5	5.7

5.3 Fixed-End Attachment

5.3.1 Drag Tests

As described in Section 3.1, the model was towed at speeds from 0.06 m/s to 0.49 m/s at the same two fill levels. Each set of conditions had six replicates. The CFD simulations were performed for the 50% and 100% full solid as described in Section 4. The results from the physical model tests and CFD simulations are shown in Figure 25.

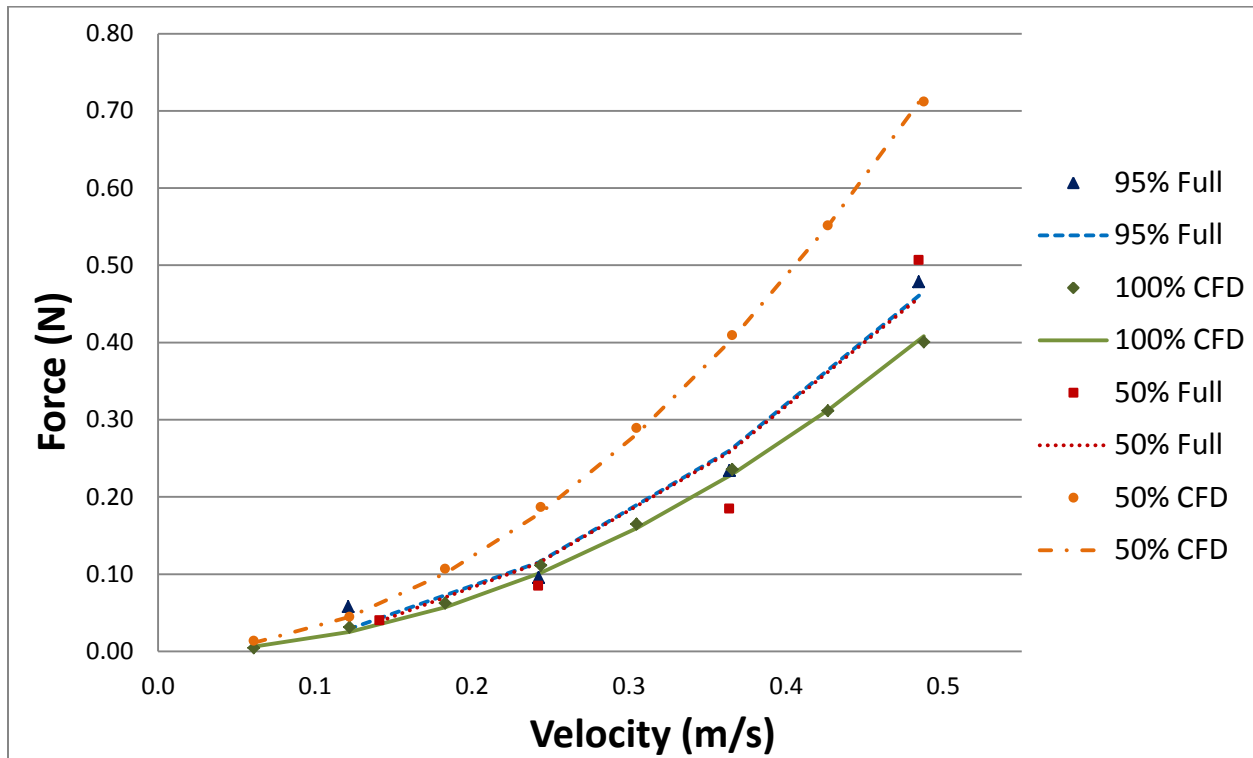


Figure 25: Fixed-end drag test results from both the physical model tests and CFD. The dotted and solid lines are the curve fit values of the individual tests (points) in the series.

Using the curve fitting approach described in Section 2.1, the C_D for was calculated for each test series. In Eq. (1), 999.8 kg/m^3 was input for ρ and the wetted surface area of the tube (0.549 m^2) was input as the reference area. The 50% and 95% full physical model tow tests produced C_D values of 0.007105 and 0.007153, respectively. Using the same technique, the

CFD simulations of 50% and 100% full cylinders yielded C_D values of 0.011030 and 0.006254, respectively. Compared to the results from the free-end tests, the results of the fixed-end drag tests did not match as well with error values of 14.4% and 35.6% for the 50% and 95% fill levels. It is likely that the attachment pipe changed the flow around the tubes, which was not represented in the CFD simulations. In addition, random and systematic uncertainty was again likely due to the small magnitude of the measured force values. For instance, the 50% full tests indicate an average of about 65% total error within the range of tests. The 95% full tests indicate an average of about 60% total error within the range of tests. For both fill levels, higher uncertainty was observed at the lower tow speeds, but the lowest total uncertainty values still ranged from 30% to 45% at the higher speeds. Conversely, the average velocity measurements indicate an average random uncertainty of less than 10%.

5.3.2 Wave Tests

At each fill level, the physical model was tested in thirteen regular and in one irregular wave condition. Six runs were performed for each set of conditions. RAO values were calculated described Section 2.2. Figure 26 shows the results from the regular and irregular wave tests with the model 50% full. Figure 27 shows the results from the regular and irregular wave tests with the model 95% full. For each of the Figures, the solid line and the circle points represent the response of the forward end cap and the dashed line and asterisks represent the response of the rear end cap of the model. In general, the results show that the response was less than one for nearly all wave frequencies.

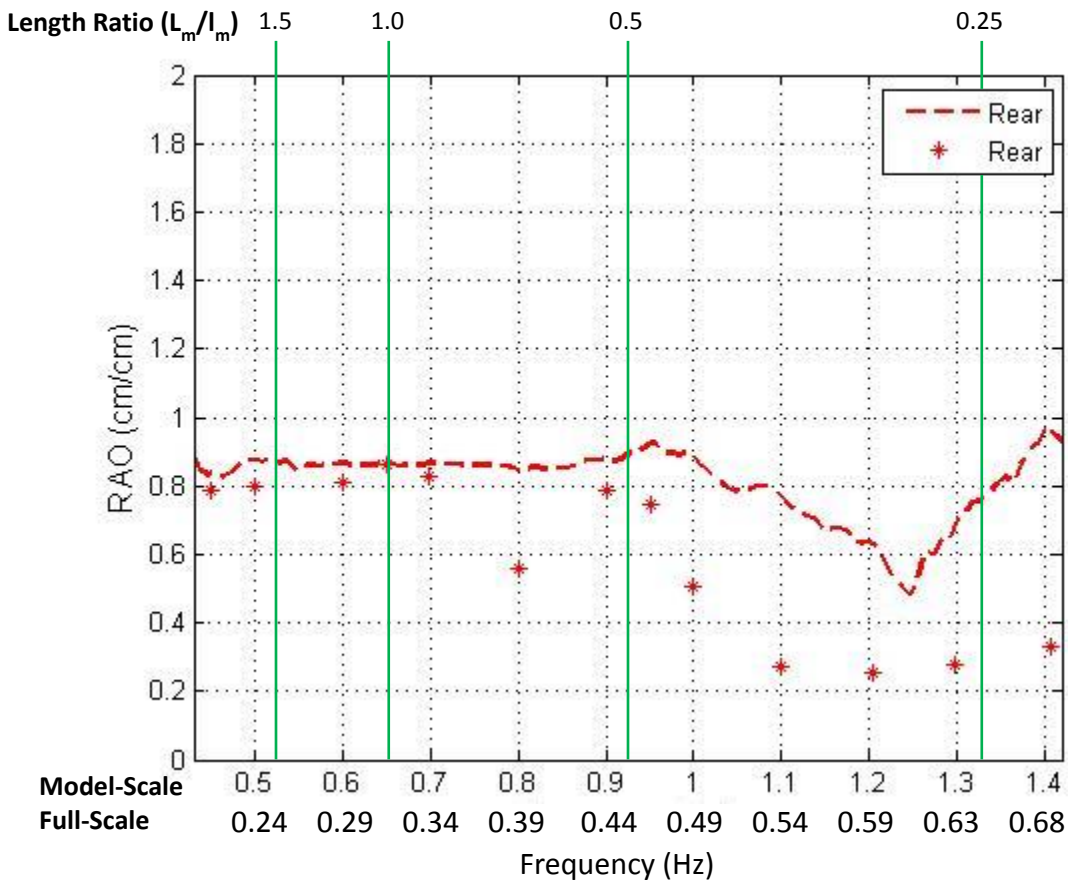


Figure 26: Fixed-end 3 MIL model response in waves (50% full). The dashed line and asterisks represent the response of the rear end cap in irregular and regular waves, respectively.

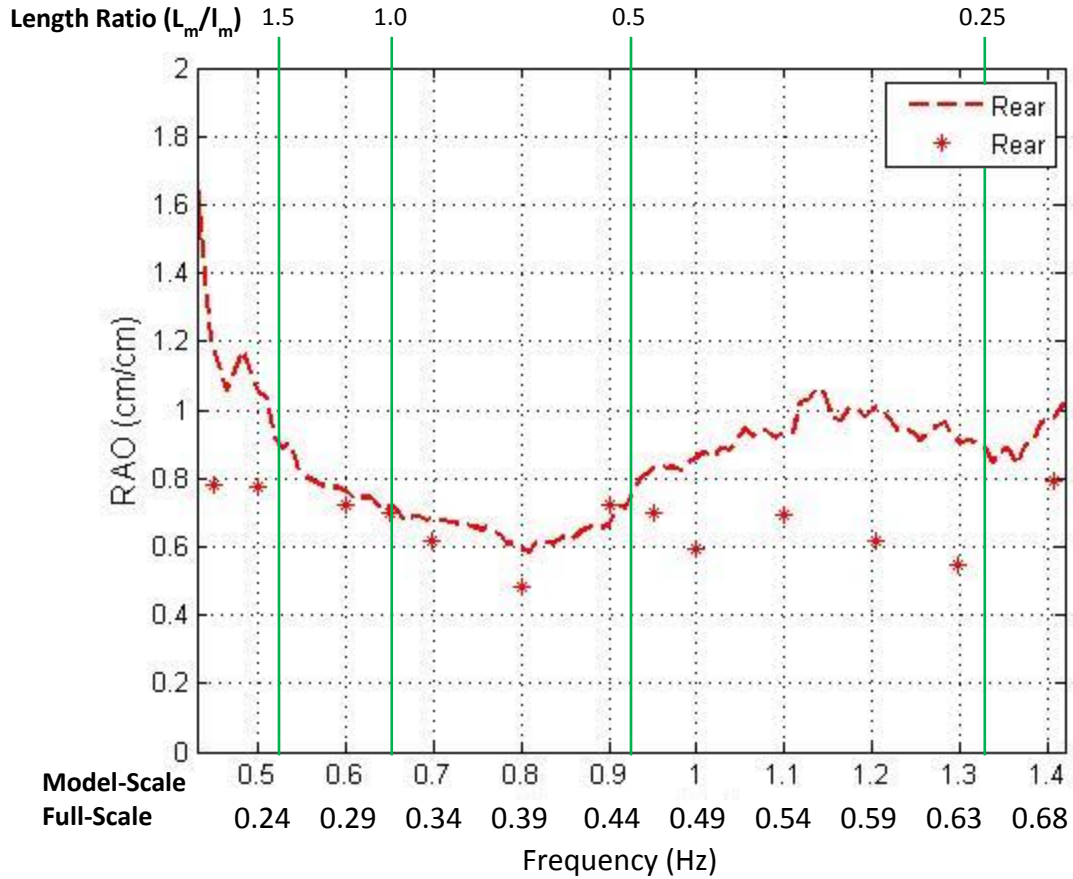


Figure 27: Free-end 3 MIL model response in waves (95% full). The dashed line and asterisks represent the response of the rear end cap in irregular and regular waves, respectively.

Like the previous models in the free-end configuration, the attachment loads were also measured throughout the testing of the fixed-end attachment style. In Figures 28 and 29, the results are presented as RAO values according to Eqs. (5), (6), and (7) in Section 2.2 for the model when 50% full and 95% full, respectively.

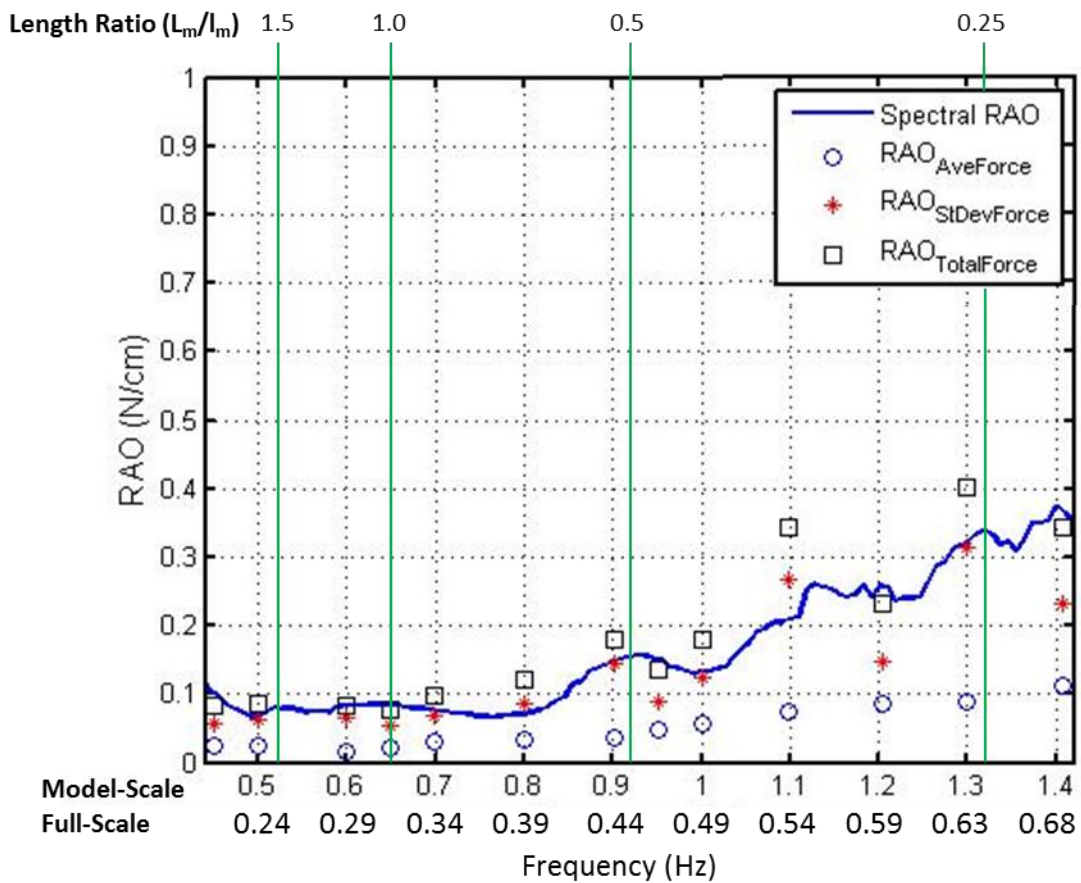


Figure 28: Fixed-end 3 MIL model response in waves (50% full). The solid line represents the spectral tension RAO. The circle points represent the average tension RAO, the asterisks represent the standard deviation RAO, and the square points represent the sum of the previous two values.

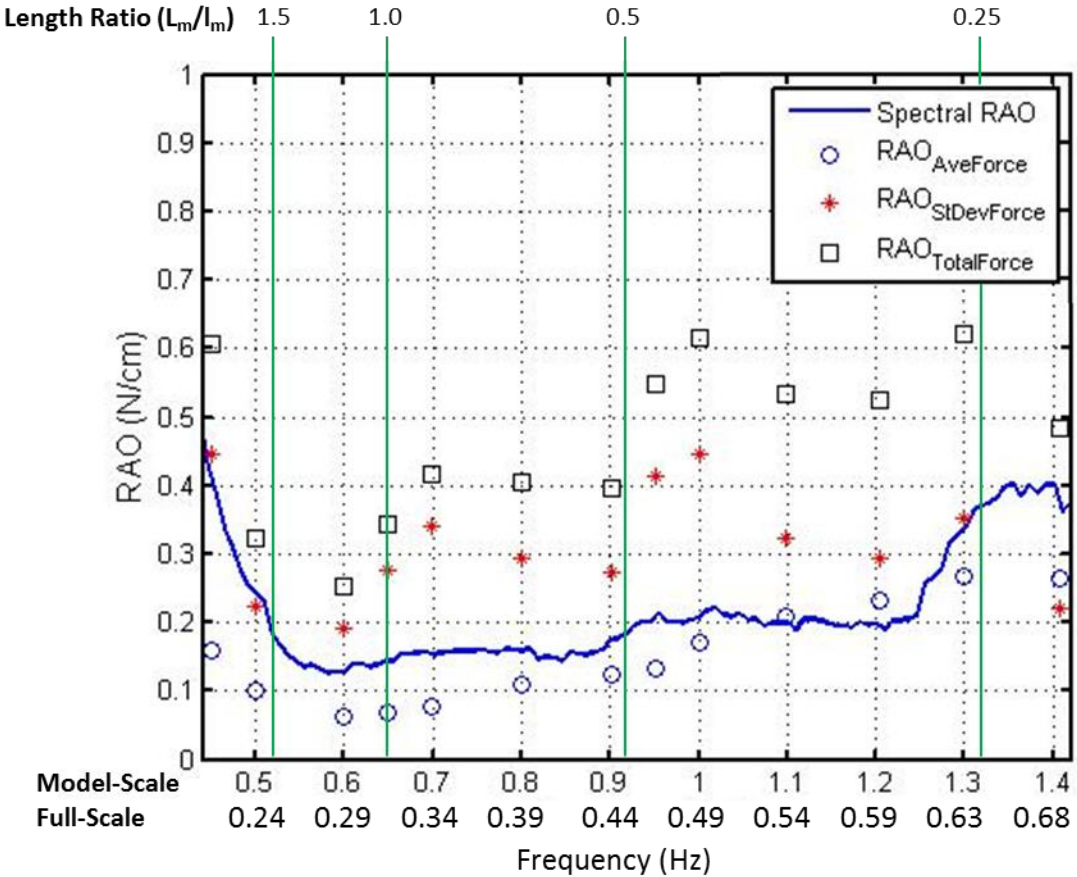


Figure 29: Fixed-end 3 MIL model response in waves (95% full). The solid line represents the spectral tension RAO. The circle points represent the average tension RAO, the asterisks represent the standard deviation RAO, and the square points represent the sum of the previous two values.

In Figure 28, the spectral tension RAO does not follow the RAO points of average force normalized over the wave amplitude as well as the previous free-end results had. In Figure 29, however, the spectral tension RAO does again tend to follow the RAO points that correlate to average force normalized by wave amplitude, just as the free-end results do. Like the previous results, both graphs also illustrate an increase in force response at higher wave frequencies.

Like the free-end wave testing, each set conditions was tested six times. Uncertainty values for each measurement were calculated as described in Section 2.3. Table 5 provides the error percentages for each measurement during testing at each fill level.

Table 5: Measurement error for 3 MIL model with fixed-end attachment in waves

Fill Level	Percent Error (%)			
	Wave Forcing	Average Tension	Tension Standard Deviation	Rear Response
50%	3.1	52.0	21.6	7.1
95%	2.7	23.0	17.0	7.4

5.3.3 Waves and Current Tests

Physical model tests were also conducted in the fixed-end attachment configuration for both fill levels in waves and currents. As described with the free-end tests, the model was towed at 0.12, 0.30, and 0.49 m/s in three sets of regular waves (0.45, 0.65, 0.95, and 1.30 Hz) and RAO values calculated. Figure 30 shows the RAO values of the wave and current tests compared to the RAO values from the wave only tests. The different symbols for the wave and current tests denote the tow velocity.

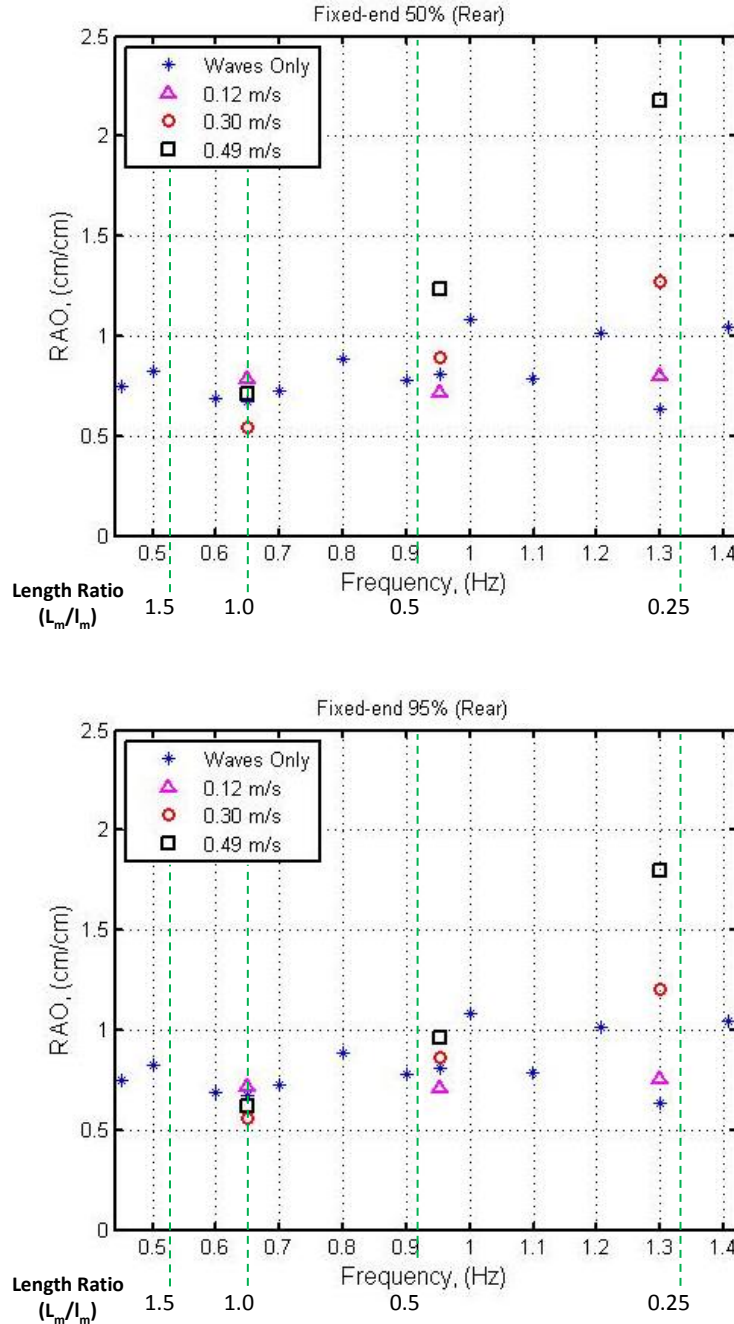


Figure 30: Wave only RAOs v. wave and current RAOs. Each graph presents the same sets of wave/current conditions. The top graph shows 50% full and the bottom shows 95% full. The three symbols stacked at the same frequency represent three different current speeds (0.12, 0.30, and 0.49 m/s) tested with waves of that particular frequency. The asterisks represent tests of waves only.

As with the free-end model, in waves with higher frequencies the addition of a current yielded a larger response at the rear end of the model. Additionally, the addition of higher

currents yielded higher responses. As well as affecting heave response, the combination of currents and various wave conditions also affect attachment loads. Figure 31 shows the attachment loads on the model filled to 50% (a) and 95% (b).

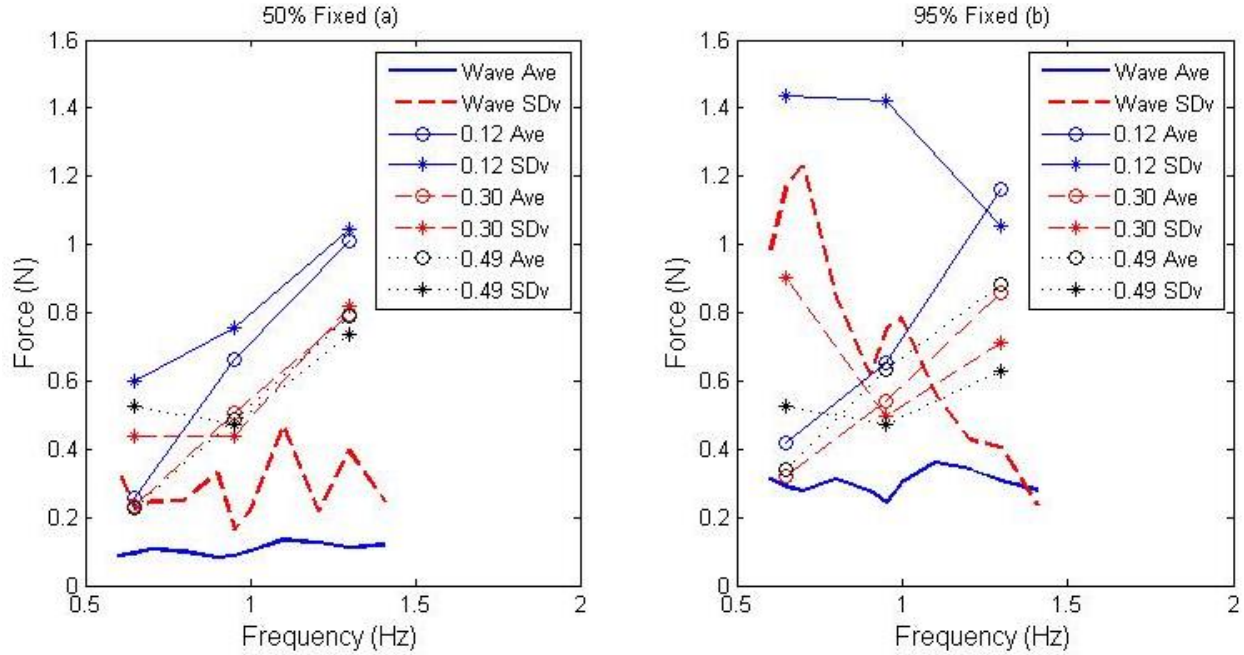


Figure 31: Attachment loads on fixed-end model filled to 50% and 95% in waves only (thick lines) and waves and current (thin lines). The circle points represent the average load and the asterisk points represent the standard deviation of the load measurements for each current velocity.

The thick lines represent the loads from tests in waves only. The thick solid line represents the average of the attachment loads and the thick dashed line represents the standard deviation of the attachment loads. Typically, the tests in waves yielded lower attachment loads than the tests conducted in similar waves with a current added. On each plot, the points connected with thin lines represent the tests of waves and currents. The circle points represent the average of the loads and the asterisk points represent the standard deviation of the loads. The points connected with a thin solid line represent wave tests with an added 0.12 m/s current, the

points connected with a thin dashed line represent wave tests with an added 0.30 m/s current, and the points connected with a thin dotted line represent wave tests with an added 0.49 m/s current.

Like the free-end tests, these tests also indicate that the average attachment loads were typically higher when the model was tested in waves and a current than in waves only. Once again, the water particle velocities associated with the wave likely contributed to the drag on the model. The attachment loads also tended to be higher in waves and currents where the waves were of a higher frequency. Additionally, like in the free-end tests, it was notable that at lower wave frequencies the standard deviation of the load (likely the force due to the waves) typically dominated the total load. At the higher frequencies, however, the relationship switched and the average of the load was often larger than the standard deviation, indicating that the towing drag force was dominating. Lastly, like the free-end results, the attachment loads were typically higher on the model when 95% full. Again, this was likely due to increased rigidity compared to the 50% full model.

Each set conditions was tested four times. Uncertainty values for each measurement were calculated as described in Section 2.3. Table 6 provides the error percentages for each measurement during testing at each fill level.

Table 6: Measurement error for 3 MIL model with fixed-end attachment in waves and currents

Fill Level	Percent Error (%)			
	Wave Forcing	Average Tension	Tension Standard Deviation	Rear Response
50%	3.7	18.2	14.6	7.3
95%	3.2	19.9	12.4	6.6

5.4 Overall Results

5.4.1 Drag Coefficients

From the physical modeling and CFD results as provided in Figures 13 and 25, it is apparent that higher fill levels may yield a smaller drag coefficient, resulting in less attachment load on the structure in flows. From the same results, there did not appear to be much drag difference between the two attachment methods. The attachment pipe likely affected the flow enough to affect the results.

5.4.2 Wave Tests

Individually, the previous wave-only RAO plots can help describe some of the trends in the data, but it is useful to juxtapose all of the data sets next to each other to investigate larger patterns. Figure 32 shows the wave-only RAO plots for all of the situations tested. From these data sets, it is apparent that the response of the models was generally higher at the front end of the tube and in waves with higher frequencies. Additionally, it seems that higher fill levels tend to increase the response observed.

In addition to these general trends, some comments can be made about specific situations. For example, the models made with 6 MIL tubing material generally had higher wave response values. The forward end response values were larger for 6 MIL case that was 95% full. The rear end of the 50% full model showed a reduced response. In both cases, the increase and decrease in response was likely due to coupling effects as a result of the stiffer construction material. Figure 32 illustrates the overall reduction in response that occurs when the leading end of the model is restricted in its motion and fixed to the attachment point.

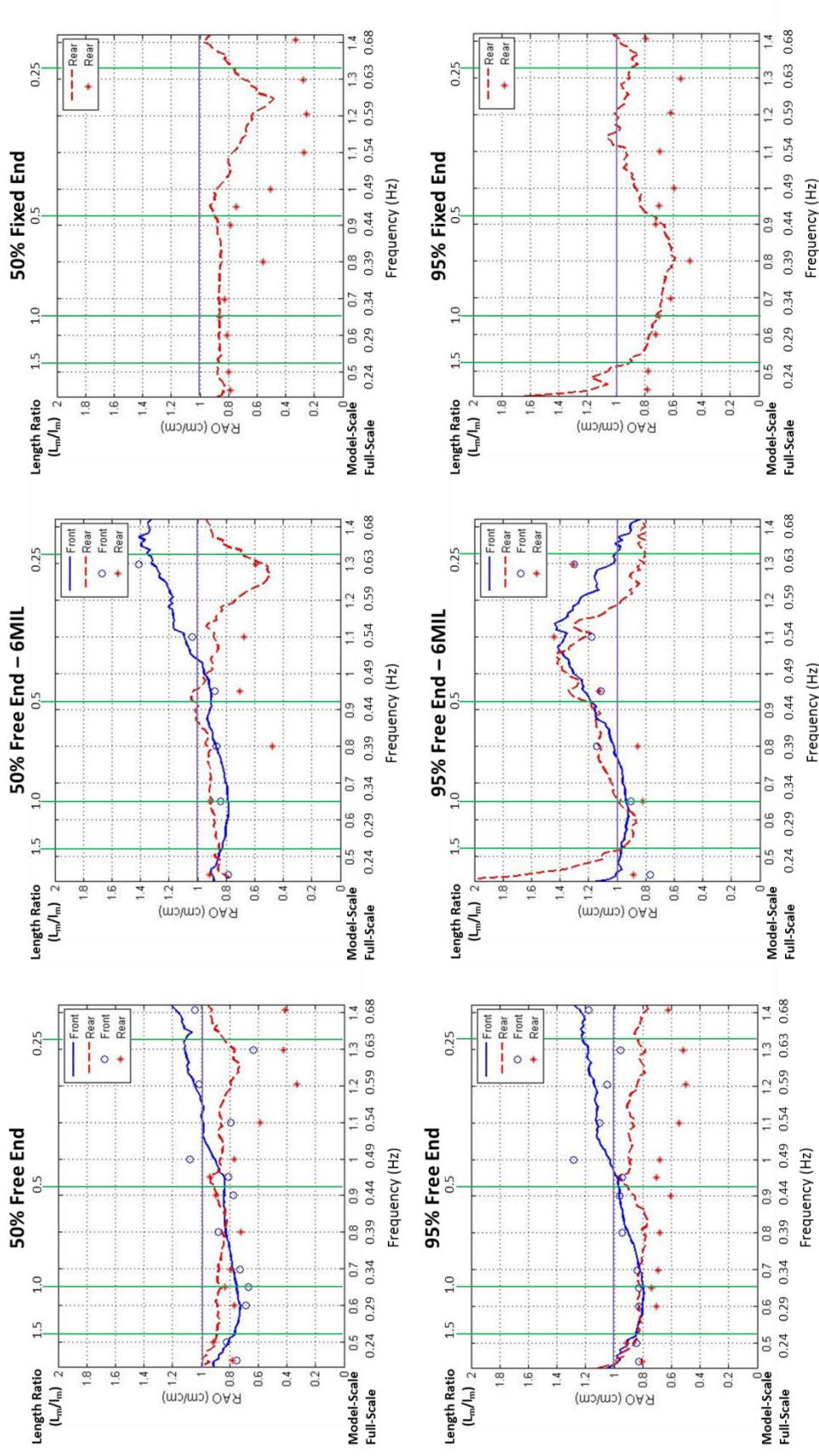


Figure 32: Wave-only RAOs for all situations. The solid lines and the circle points represent the response of the forward end cap in irregular and regular waves, respectively. The dashed lines and asterisks represent the response of the rear end cap in irregular and regular waves, respectively. Each individual graph displays results from a different fill level or attachment method.

The comparison plots on Figure 33 relate the front and rear response values. The front and rear spectral RAOs are plotted on separate graphs with each fill level and attachment configuration having its own line style. From these plots, one can observe that the 6 MIL models and the models with higher fill levels generally exhibited higher responses to the wave forcing. The forward end cap also shows a larger response in higher frequency waves. Except for the 95% full 6 MIL model, the rear end caps stayed fairly consistent in their response with values between 0.8 and 1.0. Figure 34 compares the fixed-end setup for all the tests conducted. From the data sets, it is apparent that fixing the leading end of the tube serves to decrease the response observed. At both fill levels and high and low frequencies, the fixed tube tends to display lower response values.

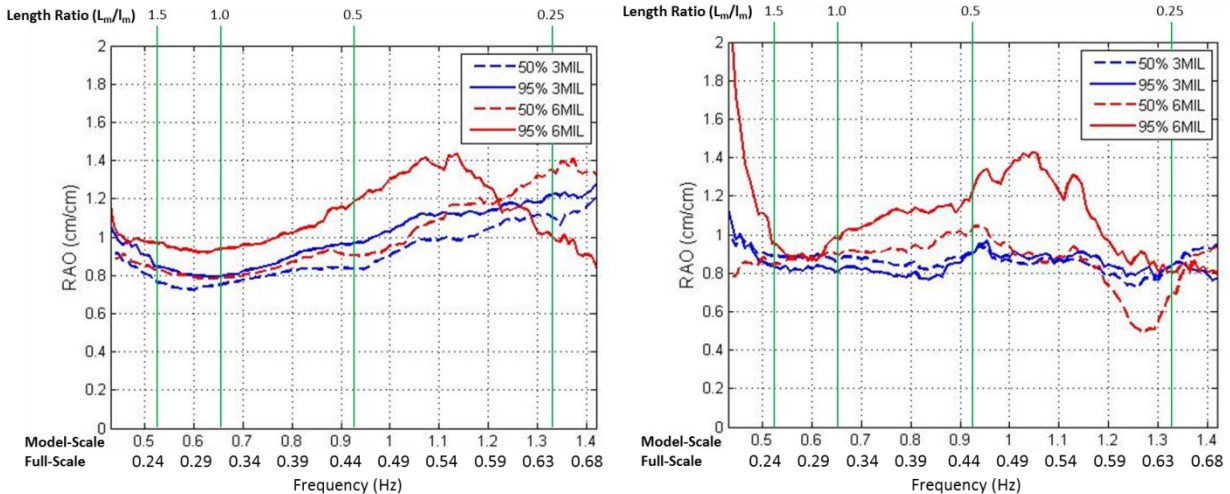


Figure 33: Forward end cap RAOs (left) and rear end cap RAOs (right). The blue lines represent 3 MIL models and the red lines represent 6 MIL models. The dashed lines represent models that are 50% full and the solid lines represent models that are 95% full.

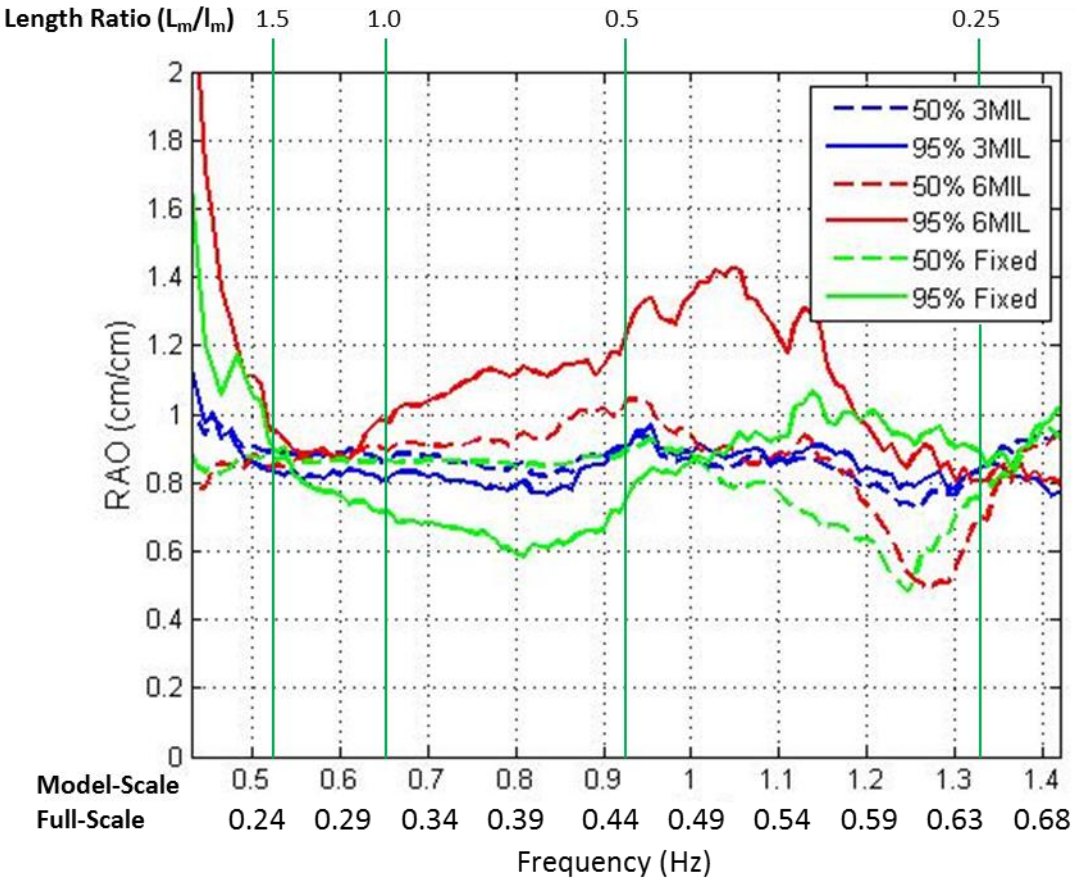


Figure 34: Rear RAOs with the addition of the RAOs from the fixed-end testing. The dashed and solid lines represent 50 and 95% fill levels, respectively. The blue and red lines represent 3 MIL and 6 MIL models, respectively. The green lines represent the results from the fixed-end model.

In Figure 35, all of the tension (attachment load) RAO plots are situated next to each other for comparison purposes. As in the previous Figures, the solid lines represent the spectral tension RAOs. The circle points represent the average tension RAO, the asterisks represent the standard deviation RAO, and the square points represent a RAO calculated with the sum of the previous two values.

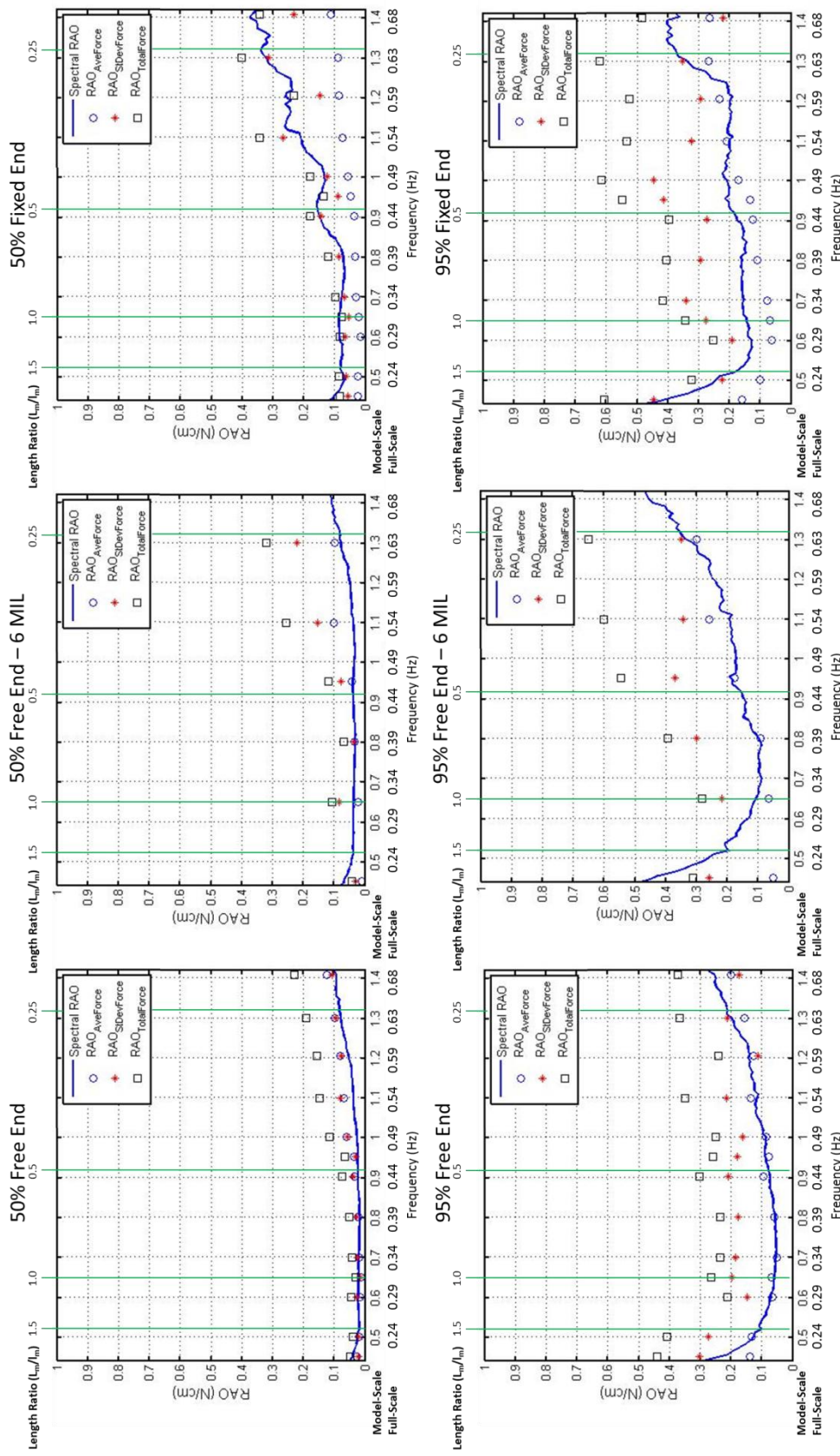


Figure 35: Wave-only attachment load (tension) RAOs for all situations. The solid lines represent the spectral tension RAOs. The circle points represent the average tension RAO, the asterisks represent the standard deviation RAO, and the square points represent the sum of the previous two values. Each individual graph displays results from a different fill level or attachment method.

Figure 35 illustrates a few notable patterns within the group of tension RAO results.

First, for all situations, the attachment loads tend to increase as wave frequency increases. The 50% fill levels when attached with a free-end method showed only a very slight correlation, but the trend still exists. Most situations also had rather low responses at frequencies under 0.44 Hz (full-scale), or what would be a wavelength to model length ratio of 0.5. Most of the responses remained at or under 0.2 N/cm, with the only exceptions being models with fixed-end attachments run in high frequency waves.

5.4.3 Wave and Current Tests

Figure 36 shows the wave only RAOs against the wave and current RAOs for each current speed. Each plot represents a different attachment method, fill level, or end cap location.

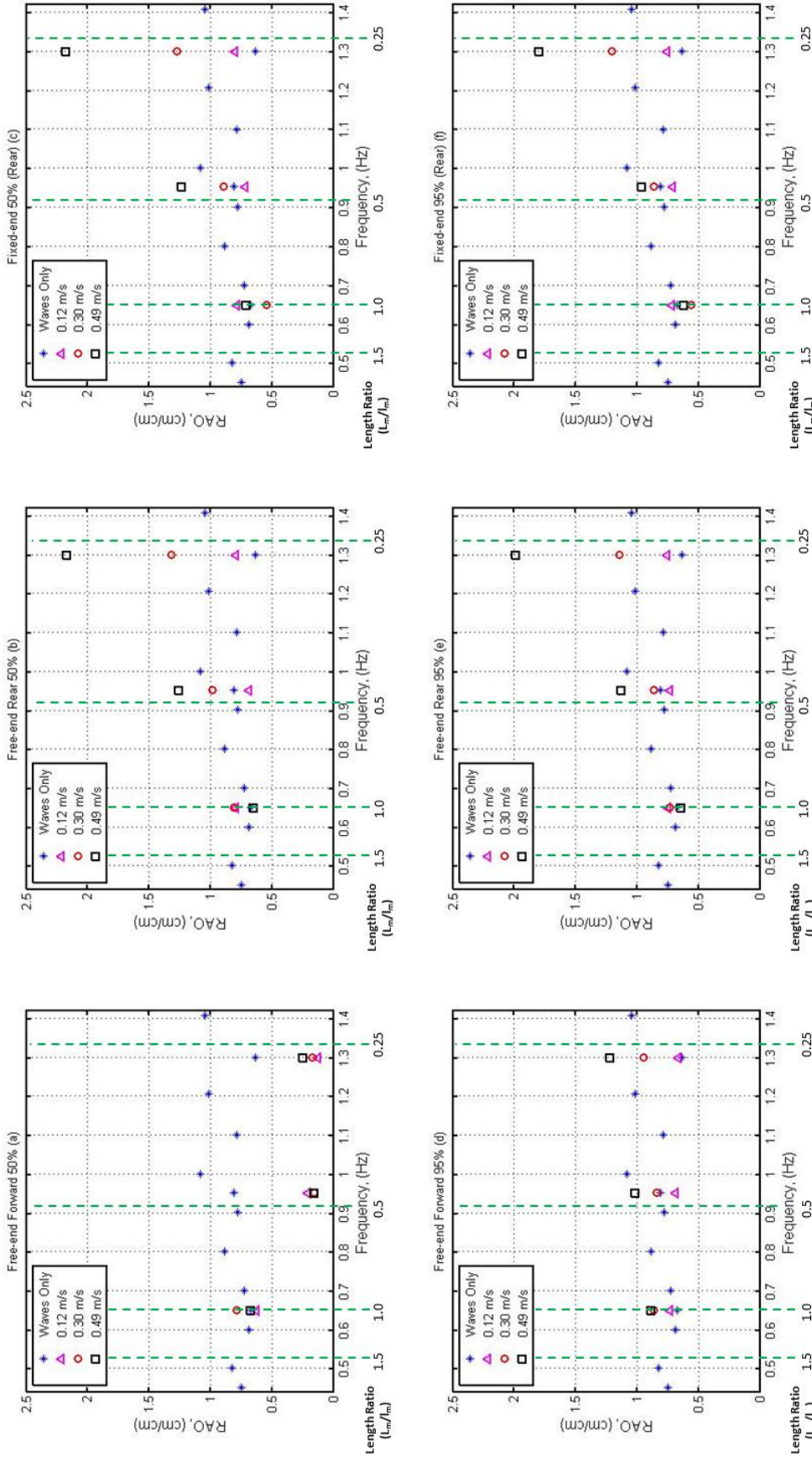


Figure 36: Wave only RAOs v. wave and current RAOs. Each graph presents the same sets of wave/current conditions. The top graphs show 50% full (a, b, c) and the bottom show 95% full (d, e, f).

The left graphs (a, c) show the front end cap response and the right graphs (b, d, e, f) show the rear end cap response.

The three asterisks stacked at the same frequency represent three different current speeds (0.12, 0.30, and 0.49 m/s) tested with waves of that particular frequency. The circles represent tests of waves only.

Figure 36 is useful for visualizing the effect that various currents have on the tube in waves. From the results, it is notable that while the front end of the tube was not affected much by the addition of the current, the response of the rear end cap tended to increase as the speed of the current increased. Additionally, the two different attachment methods did not have any noticeable effect on the response of the read end cap in waves and currents.

Figure 37 shows the attachment loads for both fill levels and both attachment techniques for waves only (thick lines) and the three wave and towing conditions (thin lines). The circle points represent the average load and the asterisk points represent the standard deviation of the load measurements. Each graph shows tests with towing speeds of 0.12, 0.30, and 0.49 m/s.

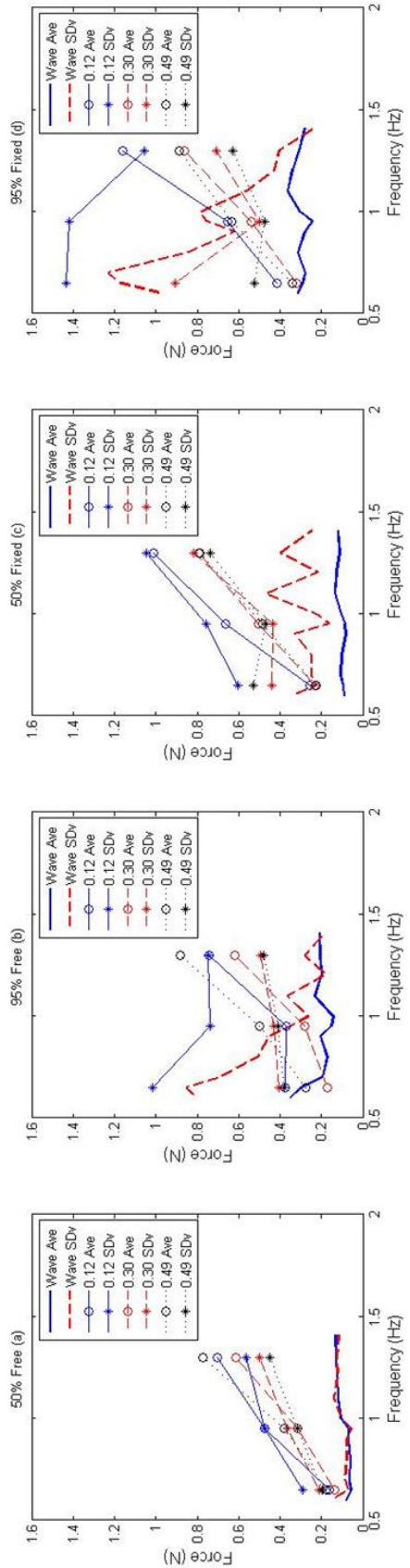


Figure 37: Attachment loads on model in waves only (thick lines) and waves and current (thin lines). The circle points represent the average load and the asterisk points represent the standard deviation of the load measurements. Each graph shows tests with towing speeds of 0.12, 0.30, and 0.49 m/s.

Figure 37 is useful for visualizing the effect of fill level, attachment technique, current velocity, and wave frequency on attachment loads. The results tend to show that a higher fill level corresponds to higher attachment loads. In addition, fixing the leading end cap can lead to higher attachment loads. It is not apparent from the results, however, that faster current speeds correlate with higher attachment loads.

By combining the information provided in both Fig. 36 and Fig. 37, several other statements can be made about the system response in waves and currents. First, it appears that higher attachment loads and responses are found in situations with waves and currents than in situations with only waves. Additionally, higher responses and higher attachment loads are associated with higher frequency waves.

6 Conclusions

6.1 Overview

Floating flexible tubes deployed in the ocean environment may be useful in addressing future energy, waste, and other concerns for society. To design and evaluate such systems effectively, however, modeling tools need to be further developed. If physical and numerical modeling techniques can consistently predict full-scale loads and response, designers will more effectively develop new systems.

6.2 Generalized Results

For this particular system, it is useful to see results indicating that the model response generally tends to follow the wave forcing. It is also important to note the specific instances when the response increases and the model follows the wave forcing less, such as at high fill levels, at high wave frequencies, when using a thicker tube material, and at the part of the model near the loaded attachment point. Other critical observations are that higher attachment loads occur when a model is in waves and a current, specifically with higher frequency waves and higher fill levels. Response also increases as wave frequency and towing speed increases. Fixing the forward end of the tube serves to slightly reduce response in waves, but it is also associated with higher attachment loads in waves and currents.

6.3 Design Suggestions and Future Work

For the proposed design, reducing response and attachment loads would likely contribute to overall survivability. Using fill levels from 50% to 90%, using as thin a material as possible

to withstand stresses, and using tubes less than half the size of the prevailing wavelengths could help reduce response in various waves conditions.

To better characterize this particular system, further research could include testing with alternate attachment configurations, additional numerical modeling, and increased testing in wider condition ranges. Future work consisting of physical tests and CFD simulations with more replicates could increase accuracy. Lastly, comparisons to large-scale model testing would assist in the development of design procedures and could validate scaling techniques.

7 References

- [1] J. Trent, P. Wiley, S. Tozzi, B. McKuln and S. Reinsch, "The Future of Biofuels: Is it in the Bag?," *Biofuels*, vol. 3, no. 5, pp. 521-524, 2012.
- [2] W. R. Hawthorne, "The early development of the Dracone flexible Barge," *Proceedings of Institution of Mechanical Engineers*, vol. 175, pp. 52 - 83, 1961.
- [3] G. Loland and J. V. Aarsnes, "Fabric as a construction material for marine applications," *Proceedings of International Conference on Hydroelasticity in Marine Technology*, 1994.
- [4] A. C. Phadke and K. F. Cheung, "Nonlinear Response of Fluid-Filled Membrane in Gravity Waves," *Journal of Engineering Mechanics*, pp. 739-750, 2003.
- [5] A. C. Phadke and K. F. Cheung, "Response of Bottom-Mounted Fluid-Filled Membrane in Gravity Waves," *Journal of Waterway, Port, Coastal, and Ocean Engineering*, pp. 294-303, 1999.
- [6] S. Das and K. F. Cheung, "Coupled boundary element and finite element model for fluid-filled membrane in gravity waves," *Engineering Analysis with Boundary Elements*, pp. 802-814, 2009.
- [7] A. C. Phadke and K. F. Cheung, "Resonance and response of fluid-filled membrane in gravity waves," *Applied Ocean Research*, pp. 15-28, 2001.
- [8] R. Zhao and J. V. Aarsnes, "Numerical and Experimental Studies of a Floating and Liquid-Filled Membrane Structure in Waves," *Ocean Engineering*, vol. 25, no. 9, pp. 753-765, 1998.
- [9] R. Zhao and M. Triantafyllou, "Hydroelastic analyses of a long flexible tube in waves,"

Proceedings of International Conference on Hydroelasticity in Marine Technology, pp. 287-300, 1994.

[10] L. L. Broderick and J. W. Leonard, "Nonlinear Response of Membranes to Ocean Waves Using Boundary and Finite Elements," *Ocean Engineering*, vol. 22, no. 7, pp. 731-745, 1995.

[11] S. F. Hoerner, Fluid-Dynamic Drag: Practical Information on Aerodynamic Drag and Hydrodynamic Resistance, New Jersey: Sighard F. Hoerner, 1965.

[12] S. K. Chakrabarti, Offshore Structure Modeling, Singapore: World Scientific Publishing Company, 1994.

[13] J. S. Bendat and A. G. Piersol, Random Data: Analysis and Measurement Procedures, New York: John Wiley and Sons, 1986.

[14] H. W. Coleman and W. G. Steele, Experimentation and Uncertainty Analysis for Engineers, New York: John Wiley & Sons, 1999.

[15] R. Zhao, "A Complete Linear Theory for a Two-Dimensional Floating and Liquid-Filled Membrane Structure in Waves," *Journal of Fluids and Structures*, no. 9, pp. 937-956, 1995.

[16] SolidWorks, "Flow Simulation 2012 Technical Reference," SolidWorks, 2012.

[17] NTNU, "TMR7 Experimental Methods in Marine Hydrodynamics – lecture in week 37," [Online]. Available: http://www.ivt.ntnu.no/imt/courses/tmr7/lecture/Scaling_Laws.pdf. [Accessed 25 November 2013].

8 Appendix A – Nomenclature

A = reference area

Ca = Cauchy number

C_D = drag coefficient

E_v = the modulus of elasticity

F_D = drag force

Fr = Froude number

g = gravitational constant

l = characteristic length

l_m = length of the model

L_m = wavelength

l_p = length of the prototype

Re = Reynolds number

U = velocity of the fluid relative to the object

λ = geometric scale ratio

μ = dynamic viscosity

ν = kinematic viscosity

ρ = density of the fluid